

# Probing the Pulsar Wind in the $\gamma$ -ray Binary System PSR B1259-63/SS 2883

Jumpei Takata<sup>1,2</sup>

takata@tiara.sinica.edu.tw

and

Ronald E. Taam<sup>1,2,3</sup>

r-taam@northwestern.edu

## ABSTRACT

The spectral energy distribution from the X-ray to the very high energy regime ( $> 100$  GeV) has been investigated for the  $\gamma$ -ray binary system PSR B1259-63/SS2883 as a function of orbital phase within the framework of a simple model of a pulsar wind nebula. The emission model is based on the synchrotron radiation process for the X-ray regime and the inverse Compton scattering process boosting stellar photons from the Be star companion to the very high energy (100GeV-TeV) regime. With this model, the observed temporal behavior can, in principle, be used to probe the pulsar wind properties at the shock as a function of the orbital phase. Due to theoretical uncertainties in the detailed microphysics of the acceleration process and the conversion of magnetic energy into particle kinetic energy, the observed X-ray data for the entire orbit are fit using two different methods. In the first method, the magnetization parameter and the Lorentz factor of the wind at the shock are allowed to vary for a given power law index characterizing the accelerated particles at the shock. In this case, the observed photon index  $\sim 1.2$  in the 1-10 keV energy band near periastron passage can be understood provided that (a) the electron energy distribution is described by a broken power law and (b) there is a break at an energy of about  $8 \times 10^6$  in units

---

<sup>1</sup>Academia Sinica Institute of Astrophysics and Astronomy-TIARA, P.O. Box 23-141, Taipei, 10617 Taiwan

<sup>2</sup>Academia Sinica Institute of Astrophysics and Astronomy/National Tsing Hua University-TIARA, Hsinchu Taiwan

<sup>3</sup>Northwestern University, Department of Physics and Astronomy, 2131 Tech Drive, Evanston, IL 60208

of the electron rest mass energy. In the second method, the magnetization parameter and the power law index are varied for a fixed Lorentz factor. Here, the photon index  $\sim 1.2$  can result from a particle distribution described by a power law index of  $\sim 1.5$ . The calculated emission in the energy band corresponding to 10 MeV-1 GeV from the shocked pulsar wind indicate that these two cases can be distinguished by future *Fermi* observations near the periastron. It is also found that the emission from the unshocked wind could be detectable by the Fermi telescope near periastron passage if most of the kinetic energy of the flow is carried by particles with Lorentz factors of  $\Gamma \sim 10^5$ .

*Subject headings:* acceleration of particles- radiation mechanisms: non-thermal-gamma rays: theory -X-rays: binaries - pulsars: individual (PSR B1259-63)

## 1. Introduction

The study of cosmic sources emitting electromagnetic radiation at very high energies in the TeV range has been greatly facilitated by the capability of ground based Cherenkov telescopes. With access to this new observational window, a class of binary systems has been recently revealed and characterized by the emission of high energy radiation. Specifically, very high energy  $\gamma$ -rays were detected from three binary systems in the Galaxy; namely, PSR B1259-63 (Aharonian et al. 2005), LS I +61° 303 (Albert et al. 2006), and LS 5039 (Aharonian et al. 2006). These  $\gamma$ -ray binaries are high mass X-ray binary systems composed of a compact object (a neutron star or black hole) in orbit around a high mass main sequence-like star (Dubus 2006b). Since very high energy emission implies the existence of charged particles in the ultra-relativistic regime, these  $\gamma$ -ray binaries can be viewed as cosmic laboratories for studies of particle acceleration.

The orbital properties of the  $\gamma$ -ray binary system associated with the Be star SS 2883 are unusual in that it has a large eccentricity ( $e = 0.87$ ) and a wide orbit with period of 1287 days. Particularly noteworthy is the presence of a young radio pulsar companion (PSR B1259-63) characterized by a spin period of  $P = 47.76$  ms and a spin down energy of  $\dot{E}_{sp} = 8 \times 10^{35}$  erg s $^{-1}$ . This system had been known as a source of non-pulsed and non-thermal emission in both the radio and X-ray energy bands (Johnston et al. 2005; Uchiyama et al. 2009), and the recent observations based on H.E.S.S. revealed the existence of very high-energy  $\gamma$ -rays (above 380 GeV) at orbital phases close to periastron passage (Aharonian et al. 2005).

PSR B1259-63/SS 2883 has also been observed to exhibit large temporal variations in its

emission and spectrum interpreted as resulting from variations in the orbital separation of the components in the system. The observational sampling of the orbit, however, is not uniform among the different wave-bands. Although the X-ray emission is measured throughout the orbit (Hirayama et al. 1996; Chernyakova et al. 2006; Uchiyama et al. 2009), the radio and the TeV emissions have been detected only during orbital phases near periastron passage (Johnston et al 2005; Aharonian et al 2005). The photon index characterizing the spectral energy distribution in the 2-10 keV band is found to vary with the orbital phase, ranging from about 1.2 to 2.

The origin of this high energy emission is likely related to the interaction of the pulsar wind of PSR B1259-63 with the outflow from the Be star (Tavani & Arons 1997). Their interaction results in the formation of a termination shock where the dynamical pressures of the pulsar wind and the stellar wind of the Be star are in balance. The shocked pulsar wind particles can emit non-thermal photons over a wide range of energies via the synchrotron radiation and inverse Compton processes. This picture for the origin of the non-thermal emission is very similar to that developed for the emission from isolated pulsars, such as the Crab pulsar (Kennel & Coroniti 1984a, b; Atoyan & Aharonian 1996). However, in this interpretation, the high energy emission regions in  $\gamma$ -ray binary systems lie close to the pulsar occurring within the orbital separation of the two components with the emission taking place in regions characterized by greater magnetic fields than those of their isolated counterparts. Specifically, the distance to the termination shock from the pulsar,  $r_s$ , in the PSR B1259-63/SS2883 system is in the range  $r_s \sim 0.1\text{--}1$  AU, and the strength of the magnetic field is in the range  $B \sim 10^{-3} \sim 0.1$  G, while  $r_s \sim 0.1$  pc and  $B \sim 100$   $\mu$ G for isolated pulsars. Therefore,  $\gamma$ -ray binaries provide a unique laboratory to probe the physics of the pulsar wind in a different regime distinct from those studies in isolated pulsars.

Within the framework of the interacting winds model, the observed temporal behavior of the flux and the photon index is caused by variations in the physical conditions at the termination shock of the pulsar wind. Because the distance of the shock from the pulsar is a function of the orbital phase, the physical properties of the pulsar wind can be probed as a function of the radial distance from the pulsar. The properties of the pulsar wind after the shock are determined by the wind magnetization parameter,  $\sigma$ , and the spin down luminosity  $\dot{E}_{sp}$  of the pulsar. The  $\sigma$  parameter is defined by the ratio of the magnetic energy to kinetic energy upstream of the shock as

$$\sigma = \frac{B_1^2}{4\pi\Gamma_1 u_1 n_1 m_e c^2}. \quad (1)$$

Here  $B_1$  and  $n_1$  are the pre shock magnetic field in the shock frame and proper number density of the electrons and positrons respectively. In addition,  $u_1$  and  $\Gamma_1 = \sqrt{1 + u_1^2}$

are the dimensionless radial four velocity and the Lorentz factor of the unshocked flow, respectively, and  $m_e$  is the rest mass of the electron and  $c$  is the speed of light. The proper number density  $n_1$  and the magnetic field  $B_1$  upstream of the shock are taken from Kennel & Coroniti (1984a, b) as

$$n_1 = \frac{\dot{E}_{sp}}{4\pi u_1 \Gamma_1 r_s^2 m_e c^3 (1 + \sigma)} \quad (2)$$

and

$$B_1^2 = \frac{\dot{E}_{sp} \sigma}{r_s^2 c (1 + \sigma)}, \quad (3)$$

respectively, where  $r_s$  is the distance of the shock from the pulsar.

At the shock, the kinetic energy of the pulsar wind is converted into the internal energy of the wind, and the distribution of downstream particles is assumed to be described by a power law over several decades in energy. For isolated pulsars, small values of the  $\sigma$  parameter have been inferred ( $\sigma \sim 0.003$ ) by Kennel & Coroniti (1984a, b), suggesting a kinetic energy dominant flow, to explain, for example, the expansion velocity of the Crab pulsar wind. It is known, however, that it is difficult to theoretically reproduce the kinetically dominated relativistic MHD flow (Bogovalov 1999), although some possible explanations for the small values for  $\sigma$  have been discussed by Kirk & Skjæraasen (2003) and Arons (2008). The resolution of the  $\sigma$  problem has yet to be clarified, as well as the acceleration mechanism at the shock. As an alternative approach, the study of the  $\gamma$ -ray binaries provides us with an astrophysical site to phenomenologically probe the  $\sigma$  parameter of the pulsar wind at varying distances from the pulsar.

The observed non-thermal emission from the radio to the very high energy band has been interpreted within the framework of a leptonic model (Tavani & Arons 1997; Kirk et al. 1999; Dubus 2006b) or in terms of a hadronic model (Neronov & Chernyakova 2007). In the leptonic model, the electrons and positrons are accelerated at the shock front and distributed over several decades in energy by a single power law index. The synchrotron emission from these particles produces non-thermal photons from the radio regime through the GeV  $\gamma$ -ray bands. On the other hand, the very high-energy ( $> 100$  GeV) photons are produced by the inverse Compton process whereby the electrons and positrons scatter optical photons from the Be star. In the hadronic model, the broad band non-thermal emission is produced as a result of collisions of protons accelerated at the shock front with the circumstellar disk. The very high energy (TeV) emission is produced via the decay of pions, while the radio to GeV emission is attributed to the synchrotron and inverse Compton processes involving the low-energy electrons and positrons produced by the decay of the charged pions.

In this paper we re-investigate the emission characteristics of the PSR B1259-63/Be star SS2883 binary system in view of recent X-ray observational data to place constraints on the

properties of the pulsar wind by further developing the synchrotron and inverse-Compton emission model for the non-thermal emission. The observations reveal that the temporal behavior of the X-ray emission predicted by Tavani & Arons (1997) is not consistent with the recent observational data. For example, the photon index  $\alpha$  was predicted to vary between  $\alpha \sim 1.5 - 2$  in the orbit, while the observed photon index is in the range  $\alpha \sim 1.2 - 1.8$ . In addition, at the very high energy bands, there is a tendency for the flux to attain a minimum at the epoch close to the periastron as observed by H.E.S.S (Aharonian et al. 2005). Although TeV emission with the leptonic model has been studied (e.g. Kirk et al. 2005; Khangulyan et al. 2007; Sierpowska-Bartosik & Bednarek 2008), the observed temporal behavior (in particular close to periastron) is not fully understood. From the theoretical perspective, we improve upon the study of Tavani & Arons (1997) by including the full corrections to the Klein Nishina cross section, following Kirk et al. (1999) and Khangulyan et al. (2007), since the inverse Compton process between the accelerated particles and the upscattered photons from the Be star occurs in a regime where such corrections can be important. Tavani & Arons (1996) carried out seminal work on the X-ray emission, but it is highly desirable to describe the temporal behavior of both the X-ray and very high-energy emission together.

The observed photon index below 1.5 in the 1-10 keV energy band is one of key observational properties requiring explanation. The present shock acceleration models (Baring 2004) predict a wide range for the power law index of the particle energy distribution ( $1.5 \lesssim p_1 \lesssim 3$ ), accommodating the observed range of the photon indices  $1.2 \lesssim \alpha \lesssim 2$ . We note that as an alternative explanation, the particle distribution described by a broken power law can reproduce the observed hard spectrum in the context of the synchrotron emission model provided that the particle distribution below the break energy is very steep. In the synchrotron spectrum, the corresponding photon energy of the break is  $E_1 = 3he\Gamma_1 B \sin \theta_p$ , where  $\Gamma_1$  is Lorentz factor at the break in the particle distribution and  $\theta_p$  is the pitch angle. For a very hard particle distribution below  $\Gamma_1$ , the photon index changes from  $\alpha = (p_1 + 1)/2$  (in the slow cooling regime) above energy  $E_1$  to  $\alpha = 2/3$  below  $E_1$ , which is the photon index in the spectral tail of the synchrotron radiation from a single particle. Therefore, if the typical photon energy  $E_1$  is larger than 10 keV, the spectrum in the 1-10 keV energy band can be characterized by a photon index less than 1.5. This interpretation may be supported by the recent SUZAKU observations, which found evidence of spectral curvature and, in particular, a spectral break around 4.5 keV (Uchiyama et al. 2009).

Accordingly, in this study, we seek to place constraints on the properties of the pulsar wind of PSR B1259-63 by developing an emission model that makes use of a stellar wind model for Be stars composed of a polar wind and an equatorial disk wind. The solution for the distribution of the particles of the shocked flow accounts for both synchrotron and inverse

Compton losses, and the neglected corrections of the Klein-Nishina scattering cross section are included. In addition to the emission from the shocked pulsar wind, we also discuss the high energy emission from the inverse Compton process operating on the unshocked wind, which scatters the optical photons from the Be star. The numerical results describing the temporal behavior of the emergent flux and power law index in the X-ray and  $\gamma$ -ray energy band over the orbit of the system are presented in §3. Finally, we discuss the results and future work in the last section.

## 2. Theoretical model

### 2.1. Stellar wind and shock distance

The dynamical pressure balance between the pulsar wind and the stellar outflow determines the location of the shock, that is,

$$\frac{\dot{E}_{sp}}{4\pi cr_s^2} = \frac{\dot{M}v_w(R_s)}{4\pi f_\Omega R_s^2} \left( \frac{v_{re}}{v_w} \right)^2, \quad (4)$$

where  $R_s = d - r_s$  is the distance of the shock from the stellar surface and  $d$  is the orbital separation between the pulsar and the star. Here, we make use of the fact that the orbital separation  $\sim 0.7 - 10$  AU and the shock distance  $\sim 0.2 - 3$  AU from the pulsar are much larger than the stellar radius,  $R_* \sim 0.05$  AU. In addition,  $\dot{M}$  and  $f_\Omega$  are the mass loss rate from the Be star and its outflow fraction in units of  $4\pi$  sr, respectively. The velocities  $v_{re}$  and  $v_w$  are the outflow velocity of the wind relative to the pulsar and its intrinsic outflow velocity. The outflow from the Be star is described by a fast low density polar wind and a slow dense equatorial disk wind (Waters 1986; Waters et al. 1988).

For the polar wind, the mass loss rate of typical early Be stars is  $\sim 10^{-9}$  to  $10^{-8}M_\odot \text{ yr}^{-1}$  (Snow 1981). We adopt the velocity field of the polar wind to be that for a radiatively driven wind given by

$$v_w(r) = v_0 + (v_\infty - v_0)(1 - R_*/R), \quad (5)$$

where  $v_0$  ( $\sim 20$  km) is the initial velocity and  $v_\infty$  is the terminal velocity, which is  $\sim 2000$  km  $\text{s}^{-1}$  for a typical Be star. Because the shock distance from the Be star is much larger than its stellar radius, we adopt  $v_w(R_s) \sim v_\infty$  at the shock. Hence, the dynamical pressure balance condition (4) leads to a shock distance

$$r_s = \frac{(\dot{E}_{sp}/cv_\infty\dot{M}_p/f_{\Omega,p})^{1/2}}{1 + (\dot{E}_{sp}/cv_\infty\dot{M}_p/f_{\Omega,p})^{1/2}}d, \quad (6)$$

where we use the condition that  $v_{re} \sim v_\infty$  because the terminal wind velocity is much greater than the typical orbital velocity of the pulsar, which is  $v_k \sim (GM_*/a)^{1/2} \sim 40 \text{ km s}^{-1}$  for a stellar mass corresponding to  $M_* \sim 10M_\odot$  and semi major axis of  $a \sim 5 \text{ AU}$ .

For the dense equatorial flow, the typical mass loss rates are of the order of  $\dot{M}_e = 10^{-7}M_\odot \text{ yr}^{-1}$  (Waters 1986), and the velocity distribution is described by

$$v_w(R) = v_0(R/R_*)^m, \quad (7)$$

where the index  $m$  is in the range of  $0 < m < 2$ , depending on the Be star (Lamers & Waters 1987). In this paper, we adopt  $m = 0.4$ , which is indicated for some Be stars (Waters 1986).

To determine the orbital phases when the pulsar wind interacts with the equatorial disk of the Be star, we make use of the radio observations. Specifically, the non-pulsed radio emission, which is likely related to the interaction between the pulsar and the disk (Ball et al. 1999), appears between  $80^\circ \lesssim \theta \lesssim 300^\circ$  where  $\theta = 180^\circ + \phi$  with  $\phi$  corresponding to the true anomaly. On the other hand, the pulsed radio emission from the pulsar magnetosphere disappears in the range  $80^\circ \lesssim \theta \lesssim 280^\circ$ . Since the eclipse is caused by absorption in the dense wind from the Be star (Johnston et al. 1992), we assume that the pulsar wind interacts with the thick equatorial disk-like outflow in the orbital phase from  $80^\circ \lesssim \theta \lesssim 300^\circ$ .

Figure 1 shows the distance to the shock front from the pulsar. The periastron is taken to be at  $\theta = 180^\circ$ . The solid and dashed lines are results for (Model 1)  $\dot{M}_p/f_{\Omega,p} = 10^{-8}M_\odot/\text{yr}$  and  $\dot{M}_e/f_{\Omega,e} = 10^{-7}M_\odot/\text{yr}$  and (Model 2)  $\dot{M}_p/f_{\Omega,p} = 10^{-9}M_\odot/\text{yr}$  and  $\dot{M}_e/f_{\Omega,e} = 10^{-8}M_\odot/\text{yr}$ , respectively. In the solid and dashed line, the discontinuities at  $\theta = 80^\circ$  and  $300^\circ$  reflect our assumption that the stellar wind discontinuously changes between the polar and equatorial winds at those orbital phases.

## 2.2. Dynamics of unshocked flow

We assume the pulsar wind to be isotropic and established beyond the light cylinder. The magnetization parameter at the light cylinder,  $\sigma_L$ , takes the value

$$\sigma_L = \frac{B_L^2}{4\pi\Gamma_L n_L m_e c^2} \sim 3 \times 10^3 \left( \frac{B_L}{10^5 \text{G}} \right) \left( \frac{R_{lc}}{10^8 \text{cm}} \right) \left( \frac{\kappa}{10^3} \right)^{-1} \left( \frac{\Gamma_L}{10^3} \right)^{-1} \quad (8)$$

in which we used  $n_L = \kappa n_{GJ}$  where  $n_{GJ}$  is the Goldreich-Julian number density at the light cylinder,  $\kappa$  is the multiplicity, and  $R_{lc}$  is the radius of the light cylinder. In pulsar models, most of the plasma is ejected from the light cylinder with a Lorentz factor  $\Gamma_L \sim 10^{2-3}$  and  $\kappa \sim 10^{2-3}$  (Daugherty & Harding 1996; Hibschan & Arons 2001), implying a magnetically

dominant flow  $\sigma_L \gg 1$ . Between the light cylinder and the terminal shock, the magnetic field may be dissipated so that the magnetic energy is converted to the particle energy of the flow (Coroniti 1990; Lyubarsky & Kirk 2001). If the magnetic energy were completely converted into the particle energy, the energy conservation implies that the terminal Lorentz factor of the bulk flow is

$$\Gamma_1 \sim \Gamma_L \sigma_L \sim 3 \times 10^6 \left( \frac{B_L}{10^5 \text{G}} \right) \left( \frac{R_{lc}}{10^8 \text{cm}} \right) \left( \frac{\kappa}{10^3} \right)^{-1}. \quad (9)$$

After complete energy conversion, most of the energy of the flow is carried by the particles with the Lorentz factor of  $\Gamma \sim \Gamma_1$ . In this case, a mono-energetic distribution,  $f(r, \Gamma) = n_1 (r_s/r)^2 \delta(\Gamma_1(r) - \Gamma)$ , or very hard distribution with a power law index (say, less than unity) between  $\Gamma_L < \Gamma < \Gamma_1$  may be applied for the energy distribution of the unshocked particles even though the pulsar wind particles are ejected from the light cylinder with a power law index larger than unity above  $\Gamma_L$  (which is expected from the of the pair-cascade process above polar cap studied by Hibschan & Arons 2001). This ultra-relativistic flow collides with the stellar wind to form a shock, where the kinetic energy of the pulsar wind is converted to the internal energy of the wind. At the shock, some electrons and positrons are further accelerated to very high energy above  $\Gamma_1$ . (§ 2.3)

The emission from the inverse Compton process of the unshocked wind can also contribute to the high energy emission from  $\gamma$ -ray binaries. For example, Ball & Kirk (2000) and Ball & Dodd (2001) computed the spectra due to the inverse Compton process from the unshocked wind with (i) a mono-energetic distribution of the electron distribution, (ii) a mono-energetic distribution of background photon fields. In this paper, we improve upon these earlier treatments by calculating spectra using the Planck distribution for the background photon field and using the differential Klein-Nishina cross section with an anisotropic photon field (also see Khangulyan et al. 2007 and Cerutti et al. 2008). In addition, to determine the sensitivity of the resulting spectrum to the input particle energy distribution, we also consider a power law distribution for the unshocked particles. The power per unit energy and per unit solid angle of the inverse Compton process is described in Takata & Chang (2007) and reference therein as

$$\frac{dP_{IC}}{d\Omega} = D^2 \int_0^{\theta_c} (1 - \beta \cos \theta_0) I_b / h \frac{d\sigma'}{d\Omega'} d\Omega_0, \quad (10)$$

where  $D = \Gamma^{-1}(1 - \beta \cos \theta_1)^{-1}$  with  $\theta_1$  and  $\theta_0$  describing the angle between the direction of the particle motion and the propagating direction of the scattered photons and background photons respectively. In addition,  $I_b$  is the background photon field and  $\theta_c = \sin^{-1} R_*/r$  expresses the angular size of the star as seen from the point  $r$ . Here,  $d\sigma'/d\Omega'$  is the differential Klein-Nishina cross section. Since the electrons and positrons of the unshocked wind lose



only about 1% of their energy by interaction with the stellar photons, we can ignore the evolution of the distribution function in the unshocked particles.

### 2.3. Dynamics of shocked flow

Following Tavani & Arons (1997), it is assumed that the electrons and positrons are accelerated to ultra-relativistic energies at a shock front that terminates the pulsar wind of PSR B1259-63. The ultra-relativistic particles injected downstream emit non-thermal radiation via the synchrotron process and the inverse Compton process, the latter involving the upscattering of the stellar optical photons of SS 2883 to the TeV energy band. For the pulsar wind, spherical symmetry is assumed. The shock distance from the pulsar is also treated as spherically symmetric to the lowest order approximation. Although the pulsar wind and stellar wind are taken to be isotropic, the geometry of the shock is anisotropic. In particular, Bogovalov et al. (2008) investigated the collision between the isotropic pulsar wind and the stellar wind in the hydrodynamical limit, finding that the geometry of the shock is a function of  $\eta \equiv \dot{E}_{sp}/c\dot{M}v_w$ . In particular, they find that the collision of the two winds produces an open shock geometry when  $\eta > 1.25 \times 10^{-2}$ . Thus, the shock geometry for the PSR B1259-63/SS 2883 system may be a function of orbital phase due to the factor,  $\eta$ , reflecting the different properties of a fast polar wind from a slow dense equatorial wind. In this case, within our level of the approximation, the inferred magnetization parameters should be considered as spherically averaged values.

For the post shock flow, the non-dimensional radial four velocity  $u_2$ , the proper number density  $n_2$ , the magnetic field  $B_2$  and the gas pressure  $P_2$  at the shock are derived using the jump conditions of a perpendicular MHD shock. For the particle kinetic energy dominant flow, that is for the low  $\sigma$  regime ( $\sigma \ll 1$ ), we obtain (Kennel & Coroniti, 1984a, b)

$$u_2 = \left( \frac{1 + 9\sigma}{8} \right)^{1/2}, \quad (11)$$

$$n_2 = \frac{n_1 u_1}{u_2}, \quad (12)$$

$$B_2 = 3B_1(1 - 4\sigma), \quad (13)$$

and

$$\frac{P_2}{n_2 u_1 m_e c^2} = \frac{1}{\sqrt{18}}(1 - 2\sigma). \quad (14)$$

For a steady state, specification of the velocity field  $u(r)$  of the downstream flow as a function of the radial distance from the shock front allows one to determine the variation of the number density and the magnetic field as a function of the radial distance. From conservation of the number flux and magnetic flux, we obtain

$$n(r)u(r)r^2 = \text{constant} \quad (15)$$

and

$$u(r)B(r)r/\Gamma_w = \text{constant}, \quad (16)$$

where  $\Gamma_w = \sqrt{1 + u^2}$  is the Lorentz factor of the shocked wind. In this study, we describe the velocity field with  $u(r) = \text{constant}$  along the flow, because (i) the high energy emission occurs in the vicinity of the shock, and (ii) recent numerical simulations in the hydrodynamical limit imply that the post shock bulk flow for the binary system does not simply decrease because of a rapid expansion of the flow in the downstream region, unlike the case for an isolated pulsar (Bogovalov et al. 2008).

To determine the distribution function of the shocked particles, we refer the procedure adopted by Kennel & Coroniti (1986a, b). Because the shock acceleration theories indicate a break in the particle energy distribution in the post-shocked flow around the injection energy (e.g. Jones & Ellison 1991; Ellison & Double 2004), we assume that the downstream particles form a broken power law distribution described by

$$f_2(\Gamma) = \frac{K_n}{4\pi} \begin{cases} \left(\frac{\Gamma}{\Gamma_1}\right)^{-p_1} & (\Gamma_1 < \Gamma \leq \Gamma_{max}) \\ \left(\frac{\Gamma}{\Gamma_1}\right)^{-p_2} & (\Gamma_{min} < \Gamma \leq \Gamma_1). \end{cases} \quad (17)$$

The maximum Lorentz factor is determined from the condition  $\Gamma_{max} = \min(\Gamma_s, \Gamma_g)$ , where  $\Gamma_s$  is the Lorentz factor for which the particle acceleration time scale  $t_{ac} \sim \Gamma_1 m_e c / e B_1$  is equal to the synchrotron radiation loss time scale,  $\tau_{sync} \sim 9 m_e^3 c^5 / e^4 B_1^2 \Gamma_1$ . Here  $\Gamma_g$  is the Lorentz factor for which the gyration radius is larger than the shock radius ( $\sim r_s$ ). For the minimum Lorentz factor  $\Gamma_{min}$ , we adopt  $\Gamma_{min} \sim \Gamma_L \sim 10^3$ , related to the Lorentz factor of the pairs produced in the magnetosphere. Our results are found to be insensitive to this choice.

The distribution function in equation (17) is described by three quantities  $K_n$ ,  $p_1$  and  $p_2$ , and we require three conditions to specify the energy distribution,  $f_2$ . However, the theoretical uncertainties in the detailed microphysics of the acceleration model preclude a determination of the power law index  $p_1$  of the accelerated particles at the shock. Thus, we take the index  $p_1$  as a model parameter ranging between 1.5 and 3. Because the distribution function  $f_2$  must satisfy the conditions  $n_2 = \int \int f_2(\gamma) d\Gamma d\Omega$  and  $\epsilon_p = m_e c^2 \int \int \Gamma f_2(\Gamma) d\Gamma d\Omega$ ,

where  $\epsilon_p$  is the energy density of the particles, we use these two conditions to calculate the two parameters,  $K_n$  and  $p_2$ . For a relativistic gas, the energy density  $\epsilon_p$  is related to the gas pressure  $P_2$  as  $\epsilon_p = 3P_2$ . On the other hand, the quantities  $n_2$  and  $P_2$  are determined by the jump condition at the shock and are calculated from equations (12) and (14) in the low  $\sigma$  regime ( $\sigma \ll 1$ ).

Note that in Kennel & Coroniti (1986a, b), a single power law distribution  $f \propto \Gamma^{-p_1}$  between  $\Gamma_{min} \leq \Gamma \leq \Gamma_{max}$  is assumed, and the normalization factor  $K_n$  and  $\Gamma_{min}$  are calculated from the two conditions on  $n_2$  and  $\epsilon_p$ . As we discussed above, however, we assumed a break in the distribution function at  $\Gamma_1$  and, alternatively, calculate the normalization factor  $K_n$  and the index  $p_2$  below the Lorentz factor  $\Gamma_1$ , because (i) the shock acceleration theories indicate a break in the particle energy distribution in the post-shocked flow around  $\Gamma_1$  and (ii)  $\Gamma_{min}$  will be related to the Lorentz factor of the pairs produced in the magnetosphere.

In the downstream region, the particles lose their energy via adiabatic expansion and radiation losses. To describe a general behavior of the time evolution of the Lorentz factor of the particles under the isotropic distribution, we integrate any angular dependences (e.g. the pitch angle and collision angle for the inverse-Compton process) and obtain

$$\frac{d\Gamma}{dt} = \frac{\Gamma}{3n} \frac{dn}{dt} - \left( \frac{d\Gamma}{dt} \right)_{syn} - \left( \frac{d\Gamma}{dt} \right)_{IC}, \quad (18)$$

where the synchrotron energy loss rate is given as

$$\left( \frac{d\Gamma}{dt} \right)_{syn} = \frac{4e^4 B^2 \Gamma^2}{9m_e^3 c^5}, \quad (19)$$

and the inverse Compton energy loss rate is

$$\left( \frac{d\Gamma}{dt} \right)_{IC} = \int \int (E - E_s) \frac{\sigma_{IC} c}{m_e c^2 E_s} \frac{dN_s}{dE_s} dE_s dE, \quad (20)$$

where  $dN_s/dE_s$  is the stellar photon field distribution from the Be star, and the cross section  $\sigma_{IC}$ , which for  $\Gamma \gg 1$ , is described by

$$\sigma_{IC} = \frac{3\sigma_T}{4\Gamma^2} \left[ 2q \ln q + (1 + 2q)(1 - q) + \frac{(\Gamma_q q)^2 (1 - q)}{2(1 + \Gamma_q q)} \right] \quad (21)$$

where  $\Gamma_q = 4\Gamma E_s/m_e c^2$ ,  $q = E_0/\Gamma_q(1 - E_0)$  with  $E_0 = E/\Gamma m_e c^2$  and  $1/(4\Gamma^2) < q < 1$  (Blumenthal & Gould 1970). With equation (18), the Lorentz factor is a function of the initial Lorentz factor  $\Gamma_2$  at the shock and the distance from the shock. From the number conservation in the phase space, the distribution function at the distance  $r$  can be calculated from

$$f(r, \Gamma) = \frac{n}{n_2} f_2 \frac{d\Gamma_2}{d\Gamma}. \quad (22)$$

Figure 2 compares the typical time scale for energy loss at the periastron due to adiabatic expansion (solid-line), synchrotron radiation (dashed-line) and inverse-Compton (dotted-line) processes as a function of the Lorentz factor. The results are for  $\sigma = 10^{-2}$  with  $\dot{M}_p/f_\Omega = 5 \cdot 10^{-9} M_\odot$  /yr and  $\dot{M}_e/f_{\Omega,e} = 5 \cdot 10^{-8} M_\odot$  /yr. We find that the adiabatic loss dominates the radiation energy losses, except for the very high energy regime ( $\Gamma > 10^8$ ), for which the synchrotron loss is more significant than the adiabatic loss (see also Khangulyan et al. 2008). The adiabatic loss dominates throughout the orbital phase, as indicated in Figure 3, which compares the various cooling time scales of the particles for a Lorentz factor  $\Gamma = 2 \times 10^6$  as a function of the orbital phase. In the case that the adiabatic loss describes the evolution of the Lorentz factor of the shocked particles, the distribution function evolves as  $f(\Gamma) \propto r_s/r$ .

For the inverse-Compton process described by the full functional form of the Klein-Nishina cross section, the cooling time scale is proportional to the Lorentz factor in the Klein-Nishina regime ( $\Gamma \geq 10^5$ ), while it is proportional to the inverse of the Lorentz factor in the Thomson regime ( $\Gamma \leq 10^5$ ). The suppression of the inverse-Compton process in the Klein-Nishina regime causes the cooling time scale of the inverse-Compton process to be much longer than that of the synchrotron process, although the energy density of the stellar photons is much larger than that of the magnetic field as Figure 4 indicates. We note that the 1-10 keV photons are emitted by the synchrotron radiation process from particles with a Lorentz factor of  $\Gamma \sim 10^6 - 10^7$  (depending on the orbital phase), indicating the particles are in slow radiation cooling regimes as Figures 2 and 3 show.

It should be noted that the mass loss rate affects the cooling time scale of the particles since the position of the shock is a function of this loss rate. To determine the relative importance of the various processes, we recast the cooling time scales as a function of the shock distance from the pulsar. In this form, the adiabatic loss time scale  $\tau_{ad} \propto 1/r_s$ , the synchrotron loss time scale  $\tau_{sync} \propto 1/r_s^{3/2}$ , and the inverse-Compton loss time scale  $\tau_{ic} \propto (d-r_s)^2$ , where the relation that Lorentz factor of the emitting particles is proportional to  $\Gamma \propto 1/B^{1/2}$  has been used for a specific energy of the synchrotron photons. Because the synchrotron radiation loss time scale is more sensitive to the shock distance than the adiabatic loss time scale, the synchrotron loss dominates others provided that the shock is located within the critical distance from the pulsar. For the X-ray emitting particles, however, one finds that the synchrotron loss dominates with the shock distance smaller than  $r_s < 2 \times 10^{-4}$  AU, providing the mass loss rate is larger than  $\dot{M} > 0.1 M_\odot$  /yr from the pulsar, which is not expected the typical mass loss rate of the Be star. On the other hand, the inverse-Compton loss may dominate at the periastron passage because the shock lies close to the Be star. For the X-ray emitting particles, inverse-Compton losses are more important if the shock is located at a distance smaller than  $R_s = d - r_s < 0.2$  AU from the Be star. The

mass loss rate for a shock distance  $R_s \sim 0.2$  AU at the periastron is  $\dot{M} \sim 2 \times 10^{-9} M_\odot$  /yr, which is lower than the typical mass loss rate of the equatorial wind, but in the range of the polar wind. In the present study, with our assumption that the pulsar wind mainly interacts with the equatorial wind at the periastron passage, the adiabatic loss processes for X-ray emitting particles dominate for the typical mass loss rates of Be stars.

In Tavani & Arons (1997), the inverse-Compton cooling time is proportional to the inverse of the Lorentz factor for the inverse-Compton process in the Klein-Nishina regime because they adopted an approximate formula for the energy loss rate of the inverse Compton process as  $\dot{\Gamma}_{IC} = \alpha_{IC} \dot{\Gamma}_T$ , where  $\dot{\Gamma}_T = c\sigma_T B \Gamma^2 / 6\pi m_e c^2$  is the energy loss rate in the Thomson limit and  $\alpha_{IC}$  is a proportionality factor. For the form used by Tavani & Arons (1997), the inverse-Compton energy loss dominates the adiabatic loss near the periastron, and the strong inverse Compton process softens the particle distribution. However, we found in Figure 2 and 3 that with the full formula of (21) of the cross section of the inverse-Compton process, the adiabatic loss is greater than the inverse-Compton loss for entire orbit. Therefore, the spectral fitting obtained in Tavani & Arons (1997) is likely to be modified using the full formula for the cross section of the inverse Compton process.

The synchrotron power per unit energy emitted by each electron is calculated from Rybicki & Lightman (1979) as

$$P_{syn}(E) = \frac{\sqrt{3}e^3 B \sin \theta_p}{hm_e c^2} F\left(\frac{E}{E_c}\right), \quad (23)$$

where  $\theta_p$  is the pitch angle,  $E_c = 3he\Gamma^2 B \sin \theta_p / 4\pi m_e c$  is typical photon energy and  $F(x) = x \int_x^\infty K_{5/3}(y) dy$ , where  $K_{5/3}$  is the modified Bessel function of order 5/3. For the pitch angle, we use the averaged value corresponding to  $\sin^2 \theta_p = 2/3$ . The power per unit energy and per unit solid angle of the inverse Compton process is described by equation (10).

For B1259-63/SS2883, the viewing geometry was determined by the observations, where the inclination angle of the plane of the orbit with respect to the sky is  $i \sim 35^\circ$  and the true anomaly of the direction of Earth is about  $\phi \sim 130^\circ$  (Johnston et al. 1996). The model spectrum of the emission from the shocked wind measured on Earth is calculated from

$$EF_E = \frac{Ee^{-\tau_{\gamma\gamma}}}{d^2} \int_{r_s}^{r^{max}} dr \int d\Gamma r^2 f(\Gamma) \left( P_{syn} + \int \frac{dP_{IC}}{d\Omega} d\Omega \right), \quad (24)$$

where  $\tau_{\gamma\gamma}$  is the optical depth for the pair-creation process. The optical depth of the photons with 100 GeV and 1 TeV propagating to the observer as a function of the orbital phase is illustrated in Figure 5 with the thick solid and dashed lines, respectively. We find from figure that the optical depth is smaller than unity, indicating the absorption of the photons propagating to the observed does not modify the level of the flux. The main reason of the

optical depth smaller than unity is the viewing geometry of the observer. For example, most of the photons propagating to direction  $i = 80^\circ$  and  $\phi = 135^\circ$  are absorbed by the stellar photons near the periastron, where the optical depth is greater than unity as indicated by thin lines in Figure 5. We integrate the emission from the shock to the distance  $r_{max} = 2r_s$ , following the result obtained by Bogovalov et al. (2008) that the emitting region, which lies between the shock and the contact discontinuity, is confined near the shock.

### 3. Results

#### 3.1. Radiation spectrum from a shocked wind

The calculated spectra from the optical to very high-energy bands at the periastron due to the shocked wind for  $\sigma = 10^{-3}$  and for a shock distance determined with Model 1 is illustrated in Figure 6. The different line types represent the results for the different photon index  $p_1$  and the Lorentz factor  $\Gamma_1$ . Specifically, the solid line, dashed line, and dash dotted line correspond to  $(p_1, \Gamma_1) = (3, 3 \times 10^6)$ ,  $(2.5, 3 \times 10^6)$ , and  $(2.5, 9 \times 10^6)$  respectively. The thin-dotted line is result for  $(p_1, \Gamma_1) = (2.5, 9 \times 10^6)$  with the pair-creation process neglected.

The calculated spectra below 100 MeV is due to synchrotron radiation, and it can be seen (see Figure 6) that the photon index of the spectrum changes at two energies around 10-100 keV and 10 MeV. The lower ( $E_1$ ) and higher ( $E_{max}$ ) energy spectral breaks correspond to the typical energies of the synchrotron radiation obtained with the Lorentz factor  $\Gamma_1$  and  $\Gamma_{max}$ , respectively. The solid and dashed-dotted lines reveal that the energy of the lower spectral break ( $E_1$ ) increases from 10 keV to 100 keV as the Lorentz factor  $\Gamma_1$  increases from  $\Gamma_1 = 3 \times 10^6$  to  $\Gamma_1 = 9 \times 10^6$ , reflecting the fact that the energy of the synchrotron photons is proportional to the square of the Lorentz factor  $\Gamma^2$ .

Between the energies  $E_1$  and  $E_{max}$ , the emission of synchrotron radiation is in the slow cooling regime (section 2.3), described by a photon index given by  $\alpha = (p_1 + 1)/2$ . For example, the photon index of the solid line in Figure 6 is about  $\alpha \sim 2$ , reflecting the power law index  $p_1 = 3$  of the electron distribution. Upon comparison of the results for the three cases in Figure 6, we find that the flux increases with (i) decreasing values of the power law index  $p_1$  of the electron distribution as indicated by the solid and dashed lines, and (ii) increasing values of the Lorentz factor  $\Gamma_1$  as indicated by the dashed and dashed-dotted lines. The former result is a consequence of the fact that more particles are distributed at higher energies for a smaller power law index. For the latter case, the energy distribution of the particles becomes harder as  $\Gamma_1$  increases, and the number of particles per unit Lorentz

factor between  $\Gamma_1 < \Gamma < \Gamma_{max}$  increases with the Lorentz factor  $\Gamma_1$ . Therefore, the flux due to synchrotron radiation between  $E_1 < E < E_{max}$  increases with the Lorentz factor  $\Gamma_1$ . On the other hand, the flux below  $E_1$  decreases with increasing values of the Lorentz factor  $\Gamma_1$  because the particles per unit Lorentz factor below  $\Gamma_1$  decrease as the particle distribution becomes harder with increasing Lorentz factor  $\Gamma_1$ . Below  $E_1$  the spectral index changes from  $\alpha = (p_1 + 1)/2$  to a very hard photon index  $\alpha = (p_2 + 1)/2$  or  $\alpha = 2/3$  if  $p_2 \leq 1/3$ .

The inverse Compton process produces the emission above 100 MeV in the spectra of Figure 6. With the typical energy of the stellar photons of  $kT \sim 2\text{eV}$ , the peak in the spectral energy distribution is located at  $(m_e c^2)^2/kT \sim 0.1\text{ TeV}$  as shown in Figure 6. Upon comparing the dashed-dotted and thin-dotted lines, we find the flux level from the inverse Compton process including the effect of the absorption process does not differ significantly from the level calculated without its inclusion. This is because the optical depth of the photons propagating toward the observer is smaller than unity for the entire orbit, as the thick-lines in Figure 5 reveal. This result is consistent with that obtained by Kirk et al. (1999) and Dubus (2006a). As shown in the dashed-dotted line, however, we can see the effects of absorption on the shape of the spectrum due to the inverse Compton process. In particular, the spectral shape with the absorption is characterized by a plateau between the spectral breaks at  $\sim 50\text{ GeV}$  and  $\sim 5\text{ TeV}$ . This is because below 50 GeV and 5 TeV, the pair creation process is ineffective.

Recently, Sierpowska-Bartosik & Bednarek (2008) argued that most of the inverse Compton photons which propagate close to the stellar surface are absorbed by the stellar photons, producing electron and positron pairs. Provided that the shock position is relatively close to the Be star, these pairs emit additional very high energy photons associated with the inverse Compton process, resulting in a pair-creation cascade. As indicated by thin-lines in Figure 5 for example, the optical depth of TeV photons emitted at a orbital phase  $\theta \sim 120^\circ$  and toward  $i = 80^\circ$  and  $\phi = 135^\circ$  is larger than unity, implying most of photons are absorbed by the stellar photons and create the secondary pairs. Because the pairs gyrate around the magnetic field lines of the Be star with a pitch angle, the pairs can emit very high energy photons in directions differing from the propagation of the primary  $\gamma$ -rays. This implies that the higher-order generated pairs may emit the  $\gamma$ -ray radiation toward the observer even though the primary  $\gamma$ -rays are not directed toward the observer. As a consequence, Sierpowska-Bartosik & Bednarek (2008) found a non negligible contribution from the pairs to the observed emission spectrum at epochs close to the periastron for PSR B1259-63/SS2883 system. Incorporating this cascade process to our model would lead to additional emission between the 50 GeV and 5 TeV energy band since the  $\gamma$ -ray absorption by the stellar photons in these energy bands is more efficient. In this case, the plateau shape of the spectra seen in Figure 6 will be modified. Although the high-order generated pairs will also emit X-ray

photons via the synchrotron radiation, which may contribute to the emission observed at the periastron passage, we have neglected these effects in our computations.

The total emission of the inverse Compton process decreases with an increase of the Lorentz factor  $\Gamma_1$  (see the dashed and dashed-dotted lines in Figure 6) as the scattering process is more efficient in the Thomson regime as compared with the Klein-Nishina regime. For the PSR B1259-64/SS2883 system, particles with Lorentz factors smaller than  $m_e c^2/kT \sim 2.5 \times 10^5$ , scatter stellar photons in the Thomson regime. This indicates that the particles in the tail ( $\Gamma < \Gamma_1$ ) of the energy distribution mainly contribute to the total emission of the inverse Compton process. Because the particle distribution becomes harder as the Lorentz factor  $\Gamma_1$  increases, the number of particles per unit energy in the tail of the distribution decreases for a given observed energy, and as a result the total emission decreases.

### 3.2. Flux in the 1-10 keV energy band

Figure 7 shows the calculated flux in the 1-10 keV energy band as a function of orbital phase. The thick-solid, dashed and dotted lines show the results for  $\sigma$  parameters of  $10^{-4}$ ,  $10^{-3}$  and  $10^{-2}$  with the shock distance calculated with  $\dot{M}_p/f_{\Omega,p} = 10^{-8}M_\odot/\text{yr}$  and  $\dot{M}_e/f_{\Omega,e} = 10^{-7}M_\odot/\text{yr}$ . The thin-solid line shows the result for  $\sigma = 10^{-4}$  with the shock distance calculated with  $\dot{M}_p/f_{\Omega,p} = 10^{-9}M_\odot/\text{yr}$  and  $\dot{M}_e/f_{\Omega,e} = 10^{-8}M_\odot/\text{yr}$ . We assume  $\Gamma_1 = 3 \times 10^6$  as the Lorentz factor of bulk motion of the unshocked wind and  $p_1 = 2.5$  as the power law index of the distribution of the accelerated particles above  $\Gamma > \Gamma_1$ . We obtained the power law index  $p_2 \sim 0.7$  for  $\Gamma < \Gamma_1$  with the method described in section 2.

By comparing the thick-solid, dashed and dotted lines, we find that the flux increases with the  $\sigma$  parameter at a given orbital phase (i.e. the same shock distance). This is simply because the magnetic field at the shock calculated from equations (3) and (13) increases with  $\sigma$ , thereby increasing the emissivity associated with synchrotron radiation. Moreover, the calculated flux in the 1-10 keV energy band tends to increase as the pulsar moves from the apastron to the periastron, that is, the luminosity is proportional to  $L_{syn} \propto 1/r_s$ . The luminosity is approximately described by  $L_{syn} \sim Vn_2P_s$ , where  $V$  is the volume of the emission region,  $n_2$  is the number density of the particles and  $P_s$  is power of synchrotron emission of a single particle. The volume of the emission region  $V$  is  $V \sim r_s^3$ , if the size of the system is less than the cooling length of the synchrotron emission. The particle number density at the shock calculated from equation (12) is proportional to  $n_2 \propto r_s^{-2}$ , and the power of the synchrotron radiation is proportional to  $P_s \propto B_2^2 \propto r_s^{-2}$ . As a result, the synchrotron luminosity is a function of the shock distance ( $L_{syn} \propto 1/r_s$ ) and increases with decreasing



radial distance of the shock from the pulsar.

A comparison of the thick- and thin-solid lines in Figure 7 describes the dependence of the synchrotron flux on the stellar wind models. Model 1 assumes a denser stellar wind model than Model 2. As Figure 1 illustrates the shock distance from the pulsar for Model 1 is about a factor of 2 smaller than that for Model 2. Since the synchrotron luminosity is related to the shock distance as  $L_{syn} \propto 1/r_s$ , the synchrotron radiation for Model 1 is about factor 2 greater than in Model 2, as shown in Figure 7.

### 3.3. Photon index in the 1-10 keV energy range

Figure 8 shows the photon index of the calculated spectrum from the particles for  $p_1 = 2.5$  in the 1-10 keV energy bands as a function of the orbital phase. The lines correspond to the same parameters as in Figure 7. We find that the photon index become smaller than 1.5 even though we have used the particle distribution with the index larger than  $p_1 > 2$ . The photon index  $\alpha$ , defined by  $dN/dE \propto E^{-\alpha}$ , decreases as the pulsar moves from the apastron to the periastron, as can be seen from Figure 8. For example, the synchrotron emission in the 1-10 keV energy band has a photon index  $\alpha \sim 1.7$  at apastron for  $\sigma = 10^{-3}$  (dashed line). This photon index follows from the relation  $\alpha = (p_1 + 1)/2$  in the slow cooling regime with  $p_1 = 2.5$ , which has been assumed in this section. On the other hand, a very hard spectrum with the photon index  $\alpha \sim 1.3$  is obtained at the periastron, reflecting the fact that the photon index in the 1-10 keV energy band is related to the energy of the lower spectral break (see §1). The energy of the lower spectral break is estimated from  $E_1 \sim 3he\Gamma_1^2 B \sin \theta_p / 4\pi m_e c$ . For  $\sigma = 10^{-3}$  and the shock distance determined with  $\dot{M}_p / f_\Omega = 10^{-8} M_\odot / \text{yr}$  and  $\dot{M}_e / f_{\Omega,e} = 10^{-7} M_\odot / \text{yr}$  (Model 1), the strength of the magnetic field is  $B_2 \sim 0.01$  Gauss at apastron and  $B_2 \sim 0.2$  Gauss at periastron. The energies,  $E_1$ , at apastron and periastron are  $\sim 1.3$  keV and  $\sim 26$  keV, where the energies are calculated with an average pitch angle  $\theta_p = \sqrt{2/3}$ . We find that near periastron, the energy of the lower spectral break is greater than 10 keV. As a result, the spectral behavior in the 1-10 keV energy band is described by the tail of the spectrum of the synchrotron radiation. In such a case, we obtain a photon index smaller than  $\alpha = 1.5$ , finding that it is possible to attain the photon index less than 1.5 with  $p_1 > 2$ .

We note that the spectrum in the 1-10 keV energy band becomes soft near the periastron in the model of Tavani & Arons (1997). Based upon the adoption of the approximate formula  $\dot{\Gamma}_{IC} \propto \Gamma^2$  for cooling, the time scale of the inverse-Compton loss for particles with Lorentz factors  $\Gamma \geq 10^6$  becomes smaller than that associated with adiabatic losses near periastron. Hence, the strong inverse Compton cooling softens the particle energy distribution and the

synchrotron spectrum in the 1-10 keV energy band such that  $\alpha \sim 2$  near periastron. In contrast, we find that with the full functional form of the scattering cross section, adiabatic losses are more significant than the inverse-Compton losses for the entire orbit. As a result, a softer spectrum near the periastron is not found in our computations, unless the pulsar wind parameters at the shock change with the orbital phase.

### 3.4. Very high-energy emissions above 380 GeV

The calculated flux integrated above 380 GeV emitted by the inverse Compton process is shown as a function of the orbital phase in Figure 9. The line types denote the same parameters as in Figure 7. The flux of the very high energy emission is not significantly affected by the value of the  $\sigma$  parameter, as we find from the thick-solid, dashed and dotted lines. However, upon comparison of the thick (Model 1) and solid (Model 2) lines we find that integrated fluxes are sensitive to the shock distance for a given orbital phase. For example, the calculated fluxes at apastron differ by about a factor of 5 even though the shock distances differ by only a factor of 2 between Model 1 and Model 2. This can be understood from the approximate form for the luminosity of the inverse Compton process given by  $L_{IC} \propto \sigma_{IC} n_2 V N_{sp}$  with  $N_{sp}$  corresponding to the number density of soft photons. If the luminosity  $L_{IC}$  is recast as a function of the shock distance, we obtain  $L_{IC} \propto r_s / (d - r_s)^2$  with  $d$  corresponding to the orbital separation. At apastron ( $d \sim 10$  AU), the shock distance from the pulsar (Figure 1) is  $r_s = 3.1$  AU for Model 1 and  $r_s = 5.9$  AU for Model 2. The ratio of the fluxes becomes  $L_{IC}(\text{Model 2}) / L_{IC}(\text{Model 1}) \sim 5.4$ , which is consistent with the ratio of calculated fluxes for Model 1 (thick-solid line) and for Model 2 (thin-solid line) in Figure 9.

It can be also seen that the very high energy emission attains a maximum value at the epoch after the periastron, although the stellar photon energy density attains a maximum value at the periastron as the dashed-line in Figure 4 shows. That is, the temporal variation with orbital phase is not symmetric with respect to the periastron. In the interaction between the pulsar and equatorial stellar winds, the outflow velocity relative to the pulsar prior to periastron ( $80^\circ \leq \theta \leq 180^\circ$ ) is  $v_{re} \sim \sqrt{v_{orb}^2 + v_w^2}$ , where  $v_w$  is the velocity of the equatorial wind taken from equation of (7), and  $v_{orb}$  is the orbital velocity of pulsar. In this case the relative velocity  $v_{re}$  is nearly constant before the periastron. From equations (4) and (7), we obtain the relation between the orbital separation and the shock distance,  $d - r_s \propto r_s^{5/6}$  with  $m = 0.4$ . The flux of the inverse Compton radiation increases,  $L_{IC} \propto r_s / (d - r_s)^2 \propto r_s^{-2/3}$ , as the pulsar approaches to the periastron. After the periastron ( $180^\circ \leq \theta \leq 300^\circ$ ), the direction of radial motion of the pulsar relative to the main star is positive so that  $v_{re} \sim$

$\sqrt{|v_{orb}^2 - v_w^2|}$ . We can see that the orbital distance and the shock distance after the periastron is related as  $d - r_s \propto r_s^{0.3}$ . As a result, we obtain  $L_{IC} \propto r_s^{0.4}$ . Thus, the inverse-Compton luminosity increases with the shock distance after the periastron in contrast to the case prior to periastron. This increase is due to the rapid change in shock distance for a small change of the orbital separation after the periastron, resulting in an increase in the emission volume with a slight decrease of the number density of the background soft photon field. This model temporal behavior provides a possible explanation of the observed fact that the flux of the very high energy photons attains a maximum value after the periastron,  $\theta \sim 270^\circ$  (§ 4.1).

The emission from the inverse Compton process of the unshocked wind can also contribute to the very high-energy emission. Figure 10 compares the temporal behaviors of integrated flux above 380 GeV from the unshocked (thick lines) and shocked (thin lines) particles. In this comparison, we have used a mono-energetic distribution for the unshocked particles. The solid and dashed lines are results for the Lorentz factor  $\Gamma_1 = 10^6$  and  $\Gamma_1 = 10^7$ , respectively. We find that the integrated flux above 380 GeV from the unshocked and shocked winds depends on  $\Gamma_1$ , decreasing with increasing Lorentz factor because the inverse Compton scattering of the pulsar wind with the black body radiation ( $kT \sim 2$  eV) from the Be star takes place in Klein-Nishina regime. As  $\Gamma_1 kT$  with  $\Gamma_1 = 10^6$  or  $10^7$  is greater than the rest mass energy of the electrons, the wind particles mainly upscatter the photons in the Rayleigh-Jeans region. Hence, the energy of incident stellar photon must lie further out in the Rayleigh-Jeans tail, corresponding to a lower photon density, to produce the very high energy photons in the case of higher Lorentz factors. Most of the soft photons above  $m_e c^2 / \Gamma_1$  are not scattered and, as a result, the number of scattered background photons, and therefore the integrated flux above 380 GeV, decreases with an increase of the Lorentz factor.

The integrated flux level from the unshocked wind is more sensitive to the Lorentz factor than from the shocked wind, as can be seen by comparing the integrated fluxes above 380 GeV of the unshocked (thick-lines) and the shocked (thin-line) wind in Figure 10. This is a direct consequence of our assumption of a mono-energetic distribution of particles for the unshocked wind and a broken power law distribution for the shocked wind. In this case, the integrated flux from the unshocked wind can be larger than from the shocked wind.

Similar temporal behavior of the integrated flux of these two components are seen in Figure 10, implying that these two components can not be distinguished based solely on the temporal behavior of the integrated flux. Furthermore, if the unshocked particles are distributed with a power law index, it will be difficult to distinguish the individual contributions, as dotted-line and thick-solid-line in Figure 11 indicate. Here, the dotted-line is the spectrum of the inverse-Compton process of the unshocked particles described by a power

law index  $p = 1$  at  $10^3 \leq \Gamma \leq 10^6$ . In this case, the particle number is uniformly distributed in the energy space, but most of the kinetic energy of the flow is carried by the particles with the Lorentz factor of  $\Gamma = 10^6$  (see § 2.2). On the other hand, it may be possible to distinguish the individual contributions if the spectral shape is measured and if the distribution of the unshocked particles is described as mono-energetic. The spectrum associated with the inverse-Compton process of the unshocked wind with the mono-energetic particle distributions are represented by the thick-solid line for  $\Gamma_1 = 10^6$  and by the thick-dashed-line for  $\Gamma_1 = 10^7$ . For an unshocked wind described by a mono-energetic distribution, the spectral shape of the inverse Compton emission has a line type structure, implying that the width of the spectrum of the high energy emission from the unshocked wind is much narrower than that from the shocked wind as already pointed out by Khangulyan et al. (2007) and Cerutti et al. (2008). A higher spectral resolution study will be required to distinguish their relative importance. For example, the solid lines in Figure 11 imply that a spectral resolution  $\delta E/E < 40\%$  at 500 GeV for  $\Gamma_1 = 10^6$  is required to distinguish between the emission from an unshocked and shocked pulsar wind.

## 4. Discussion

### 4.1. Comparison with the observations

The X-ray observations (Hirayama et al. 1996; Chernyakova et al. 2006; Uchiyama et al. 2009) provide the temporal behavior of the radiation spectrum and the photon index for the entire orbital phase. We refer to the orbital phases, where the X-ray data is available, as X1, X2, S1, A2, etc., following Chernyakova et al. (2006) and Uchiyama et al. (2009). The observed integrated flux in the 1-10 keV energy band increases by about an order of magnitude between the orbital phase  $\theta \sim 50$  degree (X6) and  $\theta \sim 100$  degree (S4). If the pulsar wind properties ( $\sigma$ ,  $\Gamma_1$  and  $p_1$ ) do not change with the orbital phase, the integrated X-ray flux in Figure 7 increases by only about factor two at the phase interval between  $\theta \sim 50$  degree and  $\theta \sim 100$  degree, implying the pulsar wind properties are a function of the orbital phase.

Uchiyama et al. (2009) fitted the X-ray data of -15 days ( $\theta \sim 95^\circ$ ), +30 days ( $\sim 291^\circ$ ) and +618 days ( $\sim 360^\circ$ ) with the synchrotron and inverse Compton radiation model, in which the adiabatic energy loss rate of the particles and the shock distance from the pulsar were parameterized. A similar computation with a parameterized adiabatic loss rate was carried out by Khangulyan et al. (2007) to explain the temporal behavior of the very high energy observations.

As an alternative interpretation of the temporal behavior, one can consider the magnetization parameter, the Lorentz factor  $\Gamma_1$  and/or the power law index  $p_1$  of the shocked particles to vary with orbital phase. In fact, it is expected that  $\sigma$  at the shock is a function of the orbital phase because the shock distance from the pulsar varies. In addition, the terminal Lorentz factor,  $\Gamma_1$ , may also vary since it depends on the multiplicity factor,  $\kappa$ , (see equation (9)), which can take different values for the different magnetic field lines accelerating the pulsar wind. In the simple model investigated by Daugherty and Harding (1996), for example, the multiplicity varies about factor of ten on the magnetic field lines coming from the polar cap region. Therefore, the fitted Lorentz factor can also be a function of orbital phase, if the observed emission in different orbital phases emanates from different field lines.

We compare the calculated flux and photon index in 1-10 keV bands with the observational results in the literature (eg. Uchiyama et al. 2009). We use the minimized  $\chi^2$  method to fit our calculated spectra in the 1-10 keV energy band with a single power law, namely,  $\alpha = (N \sum x_i y_i - \sum x_i \sum y_i) / [N \sum x_i^2 - (\sum x_i)^2]$ , where  $N$  is the number of the sampling points in the energy range  $1 \text{ keV} < E < 10 \text{ keV}$ , and  $x_i$  and  $y_i$  are the logarithm of the energy and the number flux of photons of  $i$ -th sample, respectively. The shock distances from the pulsar were taken as an average of Model 1 and Model 2 shown in Figure 1.

An example of the fit parameters is summarized in Table 1, showing  $\sigma$  and  $\Gamma_1$  with  $p_1 = 3$  at different orbital phases. Figure 12 shows the temporal behavior of the integrated flux in the 1-10 keV energy band and above 380 GeV. The temporal behavior of the photon index in the 1-10 keV energy band is shown in Figure 13. Considering the X-ray data near the apastron, we adopt  $\sigma_0 = 8 \times 10^{-4}$  at orbital phase X3 as shown in Table 1. Given this choice, a Lorentz factor  $\Gamma_1 = 8.5 \times 10^6$  provides a good fit to the observed photon index at this phase. In this case, the calculated flux at X3 is adjusted to the data with a normalization factor ( $\sim 3$ ). With this normalization factor, the integrated flux and photon index are fit to the X-ray data at other orbital phases, determining both  $\sigma$  and  $\Gamma_1$ .

We note that the value of the  $\sigma$  parameter at X3 is not arbitrarily chosen since a smaller value (e.g.  $\sigma_0 = 10^{-4}$ ) leads to a calculated flux that is too small, requiring a normalization factor that is greater than a factor of ten. On the other hand, a larger value (e.g.  $\sigma_0 = 5 \times 10^{-3}$ ) does not produce a fit to the data near the periastron (A3) for a wide range of  $\sigma$  and  $\Gamma_1$  combinations. For a shock distance corresponding to an average value determined in Models 1 and 2, we find that  $\sigma_0 \sim 8 \times 10^{-4} - 10^{-3}$  is suggested by the data in the 1-10 keV energy band.

The results in Table 1 are based on an assumed power law index ( $p_1 = 3$ ) for the particle energy distribution (see equation (17)) for the entire orbit. Such a choice was based on the

fact that (i) the observed photon indices are greater than 1.7 at and near the apastron and periastron, excluding a particle energy distribution with a very hard index, and (ii) such a choice is required to explain the observed soft spectrum  $\alpha \sim 1.95$  in the 1-10 keV energy band at orbital phase A2. We note that the observed very hard spectrum  $\alpha \sim 1.2$  at phase X7 is obtained with the power law index  $p_1 = 3$  because of (i) a spectral break larger than  $E_c > 10$  keV with the fitted Lorentz factor of  $7.8 \times 10^6$  and (ii) the very hard spectrum with  $p_2 \sim 0.45$  below  $E_c$ .

Based on the inferred parameters of the pulsar wind deduced by the X-ray observations and without any additional free parameters, the predicted very high energy emission above 380 GeV (see filled triangles in Figure 12) is found to be qualitatively consistent with the observations (vertical solid lines), except at orbital phase S6 where the predicted flux may be too large by comparing to a value extrapolated from the present H.E.S.S. observations.

The predicted flux above 380 GeV attains a maximum value after the periastron as discussed in § 3.4. LS I+61°303 also shows a similar temporal behavior to the PSR B1259-63/SS2883 system in the very high energy bands as the flux attains a maximum value after periastron. However, the cause is different from that in PSR B1259-63/SS2883 system. In particular, Sierpowska-Bartosik & Torres (2009) argue that the observed temporal behavior of LS I+61°303 is caused by the absorption of the photons near periastron, where the optical depths greater than unity are expected for the very high energy photons propagating to the observer. Therefore most of high-energy photons emitted near the periastron are absorbed by the stellar photons for LS I+61°303. In contrast, the optical depth of the photons for the PSR B1259-63/SS2883 system is smaller than unity for entire orbit (see Figure 5).

The solid line in Figure 14 represents the model spectrum for the shocked particles averaged during the 4-month time interval from -20 days ( $\theta \sim 83^\circ$ ) and +100 days ( $\theta \sim 324^\circ$ ), which was chosen for comparison with the four month observations (February - May in 2004) by H.E.S.S. We find that the predicted level of the flux is consistent with the H.E.S.S. observations below 1 TeV (Aharonian et al. 2005), while the model predicts a softer spectrum than observed above 1 TeV. On the other hand, we find that detection by the Fermi telescope is not expected at the GeV energy bands for this model. Note that the calculated spectrum averaged during the four month time interval -60 days ( $\theta \sim 48^\circ$ ) and +60 days ( $\theta \sim 312^\circ$ ) is very similar to and can not be distinguished from the solid line in Figure 14.

In summary, our phenomenological analysis places constraints on the parameters  $\sigma$  and  $\Gamma_1$  as a function of orbital phase in the  $\gamma$ -ray binary system PSR B1259-63/SS 2883. We have found that  $\sigma$  tends to increase as the pulsar companion to the Be star approaches periastron (orbital phase A2), suggesting that the energy conversion process from the magnetic field to bulk motion of the pulsar wind varies on the scale of the shock distance in the binary.

In addition, constraints on  $\Gamma_1$  have been inferred from the hardness of the spectrum. The hardening seen in the observed spectrum in Figure 13 between orbital phases X3 and X7 can be fit for Lorentz factors  $\Gamma_1$  which do not significantly vary. However, after orbital phase X7, the observed photon index returns to a value steeper than the photon index 1.2 at X7 (Figure 13), which is not easily produced by the synchrotron model for a fixed  $\Gamma_1$  throughout the orbit. As a result, the Lorentz factors near the periastron ( $\Gamma_1 \sim 3 \times 10^5$  at A2) are more than an order of magnitude smaller than that near apastron ( $\Gamma_1 \sim 8 \times 10^6$  at X3). The large variation of the fitted Lorentz factor  $\Gamma_1$  may imply that the observed emission in various orbital phases emanate from the different field lines giving rise to a range of multiplicities. The Lorentz factors from  $\Gamma_1 = 8 \times 10^6$  to  $3 \times 10^6$  correspond to the multiplicities of  $\kappa \sim 3 \times 10^3$  and  $10^2$ , respectively (see equation (9)) and are in the range predicted by pulsar models (Daugherty & Harding 1996; Hibschan & Arons 2001). Some support for this picture is provided in the simple model by Daugherty & Harding (1996), which indicates that the multiplicity changes by about a factor of 10 across the magnetic field lines emanating from the polar cap region (see figure 3 in their paper). The predicted variation for  $\Gamma_1$  ( $\sim 30$ ) in the present paper is larger than indicated in this model, but may be in an acceptable range.

Although the above fits are in reasonable accord with the observations, our lack of a physical understanding for the inferred parameter values suggests that an alternative interpretation for the observed temporal behavior be considered in order to determine the sensitivity of the fits to the particular parameterizations. Specifically, we examine the possibility that the power law index  $p_1$  of the accelerated particles varies throughout the orbit. The present shock acceleration models (e.g. Baring 2004) predict a value in the range  $1.5 \lesssim p_1 \lesssim 3$ , which can accommodate the observed ranges of the photon indices  $1.2 \lesssim \alpha \lesssim 2$ . Therefore, the X-ray data were fitted with a model parameterizing  $\sigma$  and  $p_1$ . The Lorentz factor was fixed at  $\Gamma_1 = 5 \times 10^5$ , which was chosen to follow  $\Gamma_1 = 4.5 \times 10^5$  obtained in Uchiyama et al. (2009), for the entire orbital phase. Table 2 lists the fitted  $\sigma$  parameters and power law indices  $p_1$  with the orbital phases.

It can be seen that the fitted power law indices,  $p_1$ , listed in Table 2 are less than  $p_1 = 3$  chosen for the fits in Table 1 in most phases of the orbit. For Table 1,  $p_1 = 3$  was chosen to obtain the observed softest photon index  $\alpha \sim 2$  near periastron (phase A2 in Figure 13) and harder spectra were produced by adjusting the Lorentz factors  $\Gamma_1$ . Here, the synchrotron radiation spectral break, corresponding to the break of the particle distribution at  $\Gamma_1$ , was located at energies larger than 1 keV for most of the orbital phase. In Table 2, on the other hand, the fits using an adopted Lorentz factor of  $\Gamma_1 = 5 \times 10^5$  produce a spectral break below 1 keV for the entire orbital phase. This indicates that the computed photon index in the 1-10 keV energy band behaves as  $\alpha = (p_1 + 1)/2$ , for X-ray emission via synchrotron

radiation process in the slow cooling regime. As a result, power law indices less than  $p_1 = 3$  can produce photon index fits less than  $\alpha < 2$  observed most of the orbital phase.

The solid line in Figure 15 represent the model spectrum averaged during the orbital phases from -20 days ( $\theta \sim 83^\circ$ ) and +100 days ( $\theta \sim 324^\circ$ ). Similar to Figure 14, the model spectrum in the TeV band is found to be qualitatively consistent with the observations below 1 TeV, while the model spectrum is softer than observations above 1 TeV. On the other hand, the emission from the shocked particles in the GeV band is expected to be detected by the *Fermi* telescope in such a model. For comparison with the solid line, we plot the model spectrum averaged during the four month time interval but from -60 days ( $\theta \sim 48^\circ$ ) to +60 days ( $\theta \sim 312^\circ$ ). Although the spectral shapes for the two time intervals are similar to each other, the level of the fluxes can be observed in Figure 15, in contrast to the case exhibited in Figure 14.

## 4.2. Radio emission

We have not attempted to compare the radio emission from our model with the observations since the model for the non-pulsed radio emission is more complex than that described for the  $X/\gamma$ -ray emission. In particular, it is expected that the radio waves are emitted by particles cooled to low energy ( $\Gamma \sim 10^2 - 10^3$ ) over a volume which is large compared to the emitting region of photons characterized by higher energies. That is, the properties of the radio emission are more sensitive to the cooling process, the shock geometry, and the propagation of the shocked wind than the emission in the  $X/\gamma$ -ray regime. Hence, studying the radio emission as a means to probe the properties of the shocked and unshocked pulsar wind is not as direct as for the high energy emission because the radio emitting particles no longer characterize the properties of the pulsar wind due to the radiation cooling process. A model describing the radio emission from the  $\gamma$ -ray binaries has been presented in Dubus (2006b).

## 4.3. Future perspective

Future observations of PSR B1259-63/SS 2883 with the Fermi telescope will provide further constraints on the properties of the emitting particles, especially for the non-thermal emission in the MeV-GeV energy range. For example, the Fermi telescope can constrain the electron energy distribution of the shocked wind. In comparing Figures 14 and 15, the slope of the flux distribution in the keV-GeV energy bands and the level of flux in the



MeV-GeV energy bands are sensitive to the adopted power law index  $p_1$ . In addition, the study of the temporal behavior by the *Fermi* telescope can be compared with the predicted behavior of the flux in the 0.02-100 GeV energy bands as summarized in Table 1 and Table 2. Moreover, a measurement of a spectral break for emission associated with the synchrotron radiation, predicted in the MeV-GeV energy bands, provides additional constraints on the highest energy of the accelerated particles at the shock. Fermi observations can also be used to investigate the unshocked wind as discussed in Khangulyan et al. (2007). Figure 16 summarizes the spectra of the inverse-Compton process of the unshocked particles with a mono-energetic distribution (thick lines) and with a power law distribution ( $p = 1$ ) for different Lorentz factors  $\Gamma_1$ . The various line types represent the results for the different Lorentz factor  $\Gamma_1$  with the solid, dotted and dotted-dashed lines corresponding to the results for  $\Gamma_1 = 10^5$ ,  $10^6$  and  $10^7$ . Here, the calculated spectra are results for the averaged spectra during the three-month time interval at the periastron passage. We find from Figure 16 that the emission from the unshocked wind could be detectable by the Fermi telescope if most of the kinetic energy of the flow is carried by the particles with the Lorentz factor of  $\Gamma \sim 10^5$ .

We have shown that both the shocked and unshocked pulsar wind can contribute to the very high energy emission and that higher spectral resolution studies will be required to distinguish their relative importance. If the energy distribution of the unshocked wind particles are described by a power law, it is difficult to distinguish those two components. However, it may be possible to distinguish the individual contributions if the distribution of the unshocked particles is described as mono-energetic, which produces a line type structure of the spectrum for the inverse Compton emission. It is found that the width of the spectrum of the high-energy emission from the mono-energetic wind particles becomes increasingly narrow for larger Lorentz factors, implying higher spectral resolution is required for larger  $\Gamma_1$ . For example, a spectral resolution  $\delta E/E < 40\%$  at 500 GeV for  $\Gamma_1 = 10^6$  would be required to distinguish between the emission from the unshocked and shocked pulsar wind.

Finally, we point out that the phenomenological approach adopted in this paper has the potential to place constraints not only on the pulsar wind properties, but also on the properties of the stellar wind from the Be star in SS 2883. For example, the index  $m$  characterizing the velocity distribution of the equatorial outflow (see equation 7) in SS 2883 is not well constrained by the observations. However, the very high energy emission above 380 GeV is a function of  $m$  with the flux decreasing for larger values of  $m$  as a consequence of the closer proximity of the termination shock to the pulsar. This follows from the fact that (i) the photon number density of the stellar radiation field decreases at the shock due to the smaller solid angle of the Be star as seen from the shock, and (ii) the high energy particles lose their energy faster via the synchrotron radiation with a stronger magnetic field at the shock. With these two effects, the very high energy emission above 380 GeV decreases

for larger values of  $m$ . Specifically, taking  $m = 1.25$ , which is used in Sierpowska-Bartosik & Bednarek (2008) in contrast to  $m = 0.4$  adopted in this paper, the predicted integrated flux above 380 GeV after periastron passage (at the orbital phase A3) is decreased by about a factor of 3. Hence, the dependence of the high energy integrated flux on the outflow index  $m$  may provide an additional diagnostic to probe the outflow index  $m$ . However, the uncertainties in the current observations preclude the usefulness of this diagnostic to discriminate the outflow indices at present. Therefore, observations at higher sensitivity as well as more sophisticated theoretical models will be necessary to realize this potential.

We wish to express our thanks to the referee for detailed comments which significantly improved the paper. In addition we also thank R.Huang for providing XMM-Newton and ASCA data. This work was supported by the Theoretical Institute for Advanced Research in Astrophysics (TIARA) operated under Academia Sinica and the National Science Council Excellence Projects program in Taiwan, administered through grant NSC 96-2752-M-007-007-PAE.

## REFERENCES

- Aharonian, F. et al. 2005, *A&A*, 442, 1
- Aharonian, F. et al. 2006, *A&A*, 460, 743
- Albert, J. et al. 2006, *Sci*, 312, 1771
- Amato, E., & Arons, J. 2006, *ApJ*, 653, 325
- Arons, J. 2008, *AIP Conference Proceedings*, 983, 200
- Atoyan, A.M., & Aharonian, F.A. 1996, *MNRAS*, 278, 525
- Ball, L., Melatos, A., Johnston, S., & Skjæraasen, O. 1999, *ApJL*, 514, 39
- Ball, L. & Kirk, J.G. 2000, *APh*, 12, 335
- Ball, L. & Dodd, J. 2001, *PASA*, 18, 98
- Baring, M.G. 2004, *Nucl. Phys. B*, 136, 198
- Blumenthal, G.R., & Gould, R.J. 1970, *Rev. Mod. Phys.*, 42, 237
- Bogovalov, S. V. 1999, *A&A*, 349, 1017

- Bogovalov, S.V., Khangulyan, D.V., Koldoba, A.V., Ustyugova, G.V. & Aharonian, F.A. 2008, MNRAS, 387, 63
- Cerutti, B., Dubus, G., & Henri, G. 2008, A&A, 488, 37
- Chernyakova, M., Neronov, A., Lutovinov, A., Rodriguez, J., & Johnston, S. 2006, MNRAS, 367, 1201
- Daugherty, J.K. & Harding, A.K. 1996, ApJ, 458, 278
- Dubus, G. 2006a, A&A, 451, 9
- Dubus, G. 2006b, A&A, 456, 801
- Ellison, D.C. & Double, G.P. 2004, APh, 22, 323
- Hirschman, J.A. & Arons, J. 2001, ApJ, 560, 871
- Hirayama, M., Nagase, F., Tavani, M., Kaspi, V.M., Kawai, N., & Arons, J. 1996, PASJ, 48, 833
- Johnston, S. et al. 1992, ApJL, 387, 37
- Johnston, S., Manchester, R.N., Lyne, A.G., D’Amico, N., Bailes, M., Gaensler, B.M. & Nicastro, L. 1996, MNRAS, 279, 1026
- Johnston, S., Ball, L., Wang, N., & Manchester, R.N. 2005, MNRAS, 358, 1069
- Jones, F.C., Ellison, D.C. 1991, Space Sci. Rev., 58, 259
- Kennel, C.F., & Coroniti, F.V. 1984a, ApJ, 283, 694
- Kennel, C.F., & Coroniti, F.V. 1984b, ApJ, 283, 710
- Khangulyan, D., Hnatic, S., Aharonian, F., & Bogovalov, S. 2007, MNRAS, 380, 320
- Khangulyan, D. V., Aharonian, F. A., Bogovalov, S. V., Koldoba, A. V., & Ustyugova, G. V. 2008, IJMPD, 17, 1909
- Kirk, J. G., Ball, L., & Skjæraasen O. 1999, APh, 10, 31
- Kirk, J. G., Ball, L., & Johnston, S. 2005, AIP Conference Proceedings, 801, 286
- Kirk J. G. & Skjæraasen O. 2003, ApJ, 591, 366
- Lamers, H.J.G.L.M., & Waters L.B.F.M. 1987, A&A, 182, 80

- Neronov, A., & Chernyakova, M. 2007, *Ap&SS*, 309, 253
- Rybicki, G. B., & Lightman, A. P. 1979, *Radiation Processes in Astrophysics* (New York: Wiley)
- Sierpowska-Bartosik, A. & Bednarek, W. 2008, *MNRAS*, 385, 2279
- Sierpowska-Bartosik, A. & Torres, D.F. 2009, *ApJ*, 693, 1462
- Snow, T.P. 1981, *ApJ*, 251, 139
- Takata, J., & Chang, H.-K. 2007, *ApJ*, 670, 677
- Tavani, M., & Arons, J. 1997, *ApJ*, 477, 439
- Uchiyama, Y., Tanaka, T., Takahashi, T., Mori, K., & Nakazawa, K. 2009 *ApJ* in press (astro-ph 0904.1238)
- Waters, L.B.F.M. 1986, *A&A*, 162, 121
- Waters, L.B.F.M., van den Heuvel, E.P.J., Taylor, A.R., Habets, G.M.H.J. & Persi, P. 1988, *A&A*, 198, 200

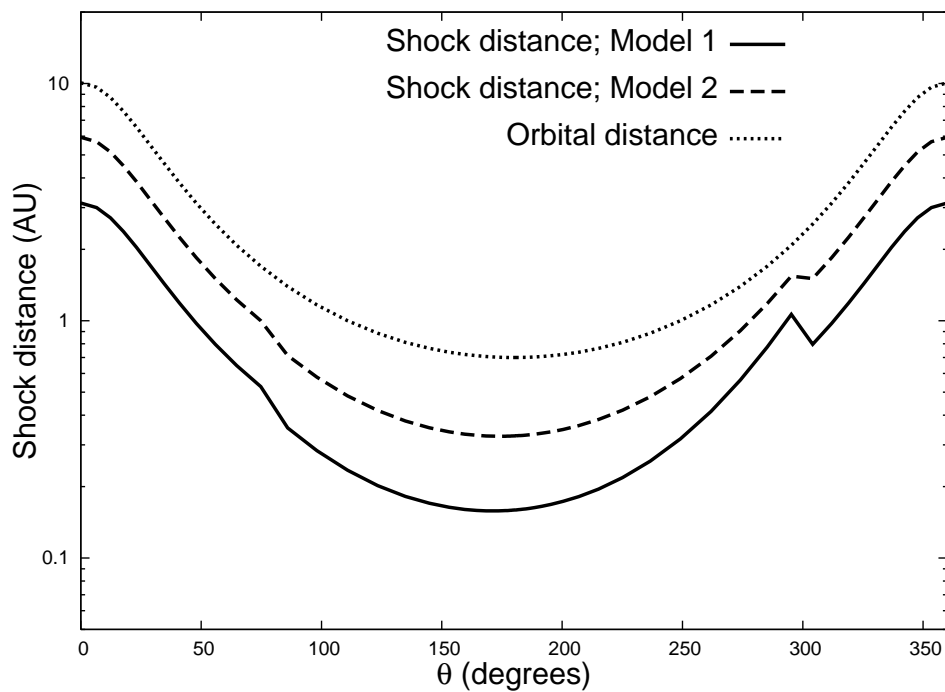


Fig. 1.— Calculated shock radius as a function of the orbital phase ( $\theta = \phi + \pi$ ). Model 1 (solid line);  $\dot{M}_p/f_\Omega = 10^{-8}M_\odot$  /yr and  $\dot{M}_e/f_{\Omega,e} = 10^{-7}M_\odot$  /yr. Model 2 (dashed line);  $\dot{M}_p/f_{\Omega,p} = 10^{-9}M_\odot$  /yr and  $\dot{M}_e/f_\Omega = 10^{-8}M_\odot$  /yr. The dotted line shows the orbital distance.

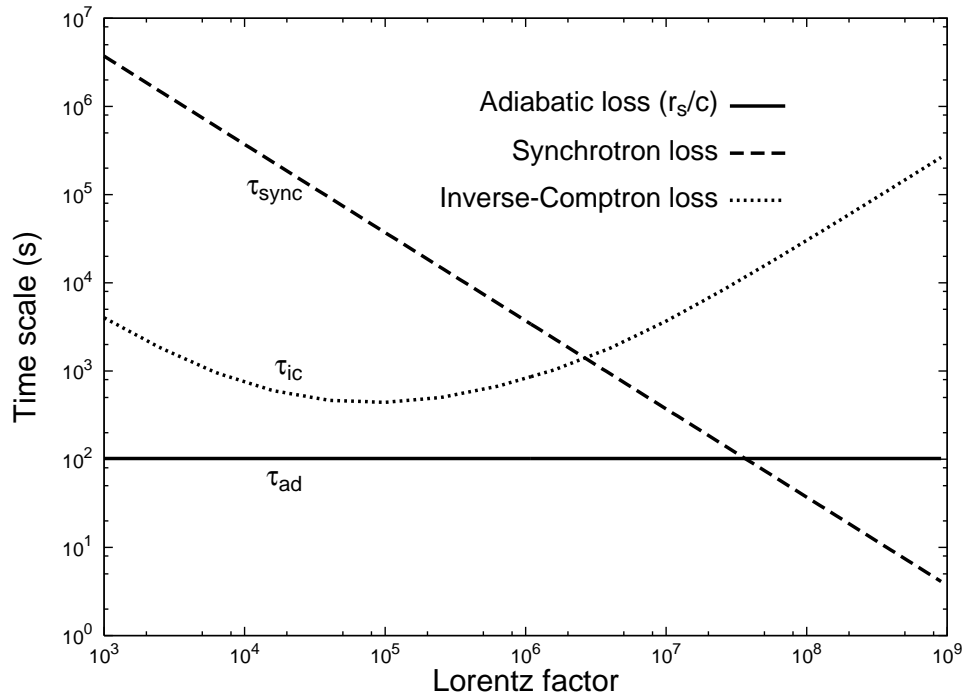


Fig. 2.— The time scale of the adiabatic loss (solid-line), the synchrotron loss (dashed-line) and the inverse-Compton loss (dotted-line) at the periastron as a function of the Lorentz factor. The results are for  $\sigma = 10^{-2}$  with  $\dot{M}_p/f_\Omega = 5 \cdot 10^{-9} M_\odot / \text{yr}$  and  $\dot{M}_e/f_{\Omega,e} = 5 \cdot 10^{-8} M_\odot / \text{yr}$ .

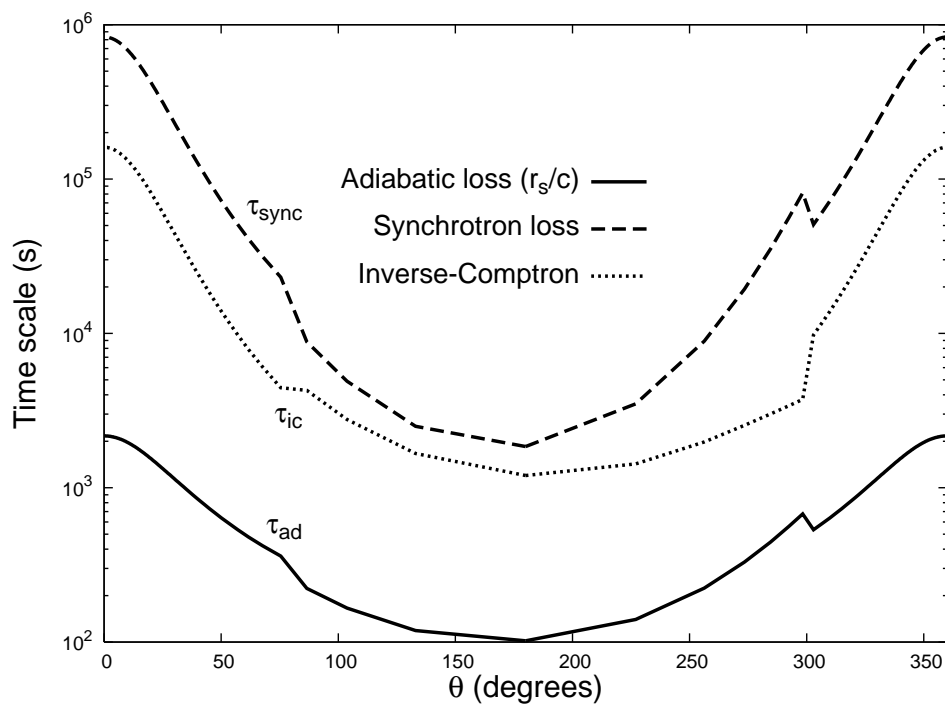


Fig. 3.— The time scales of the energy loss for the particles with the Lorentz factor  $2 \times 10^6$  as a function of the orbital phase. The results are for  $\sigma = 10^{-2}$  with  $\dot{M}_p/f_\Omega = 5 \cdot 10^{-9} M_\odot / \text{yr}$  and  $\dot{M}_e/f_{\Omega,e} = 5 \cdot 10^{-8} M_\odot / \text{yr}$ .

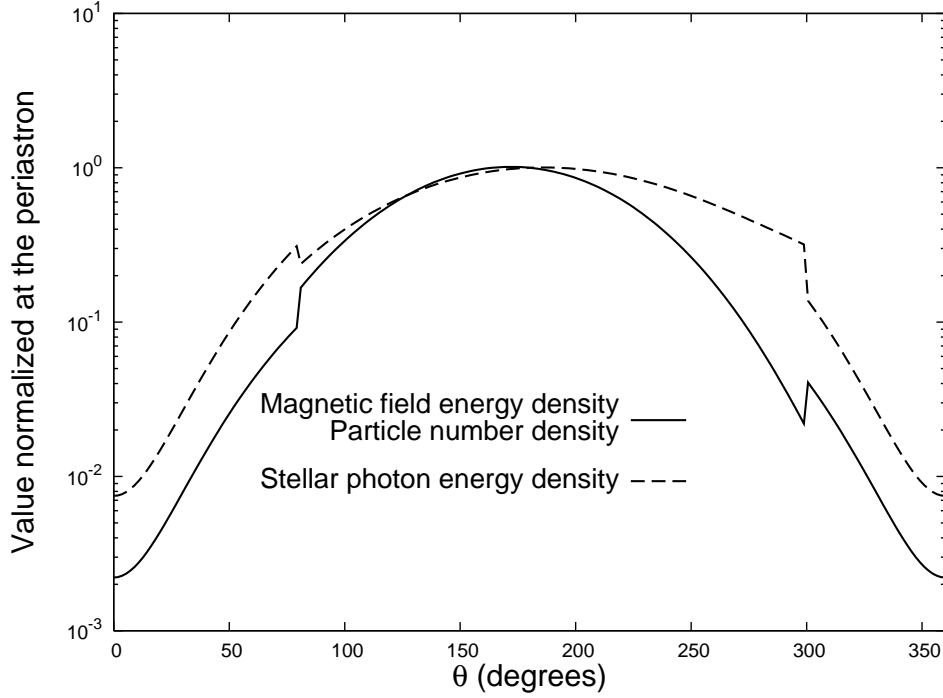


Fig. 4.— Variation of the magnetic field energy and particle number density (solid line), which evolve as  $\propto 1/r_s^2$ , and the stellar photon energy density (dashed line) at the shock. The curves of the magnetic field density and the particles number density, which are proportional to the inverse square of the shock distance  $\propto r_s^2$ , overlap in the figure. The values are normalized at the periastron, where the magnetic field energy, the particle number density and the stellar photon energy density are  $\sim 0.018 \text{ erg/cm}^3$ ,  $\sim 0.37 \text{ /cm}^3$  and  $\sim 34 \text{ erg/cm}^3$ , respectively. The results are for  $\sigma = 10^{-2}$  with  $\dot{M}_p/f_\Omega = 5 \cdot 10^{-9} M_\odot \text{ /yr}$  and  $\dot{M}_e/f_{\Omega,e} = 5 \cdot 10^{-8} M_\odot \text{ /yr}$ .



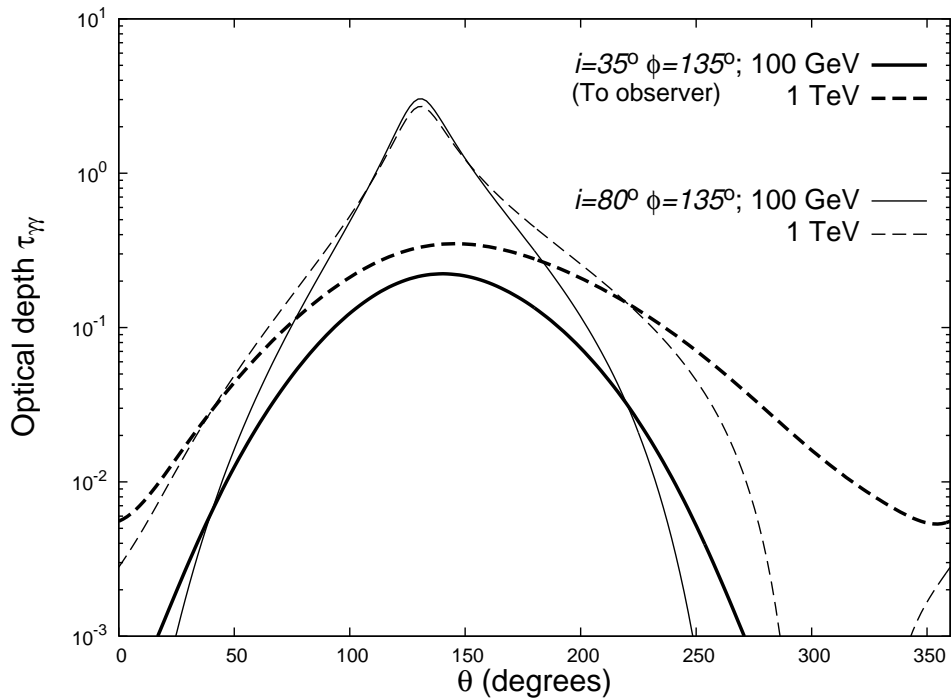


Fig. 5.— Optical depth associated with the creation of pairs by photons with energy 100 GeV (solid-lines) and 1 TeV (dashed-lines). The thick and thin lines represent the results for the photons propagating to the observer  $(i, \phi) = (35^\circ, 130^\circ)$  and the direction with  $(80^\circ, 130^\circ)$ , respectively.

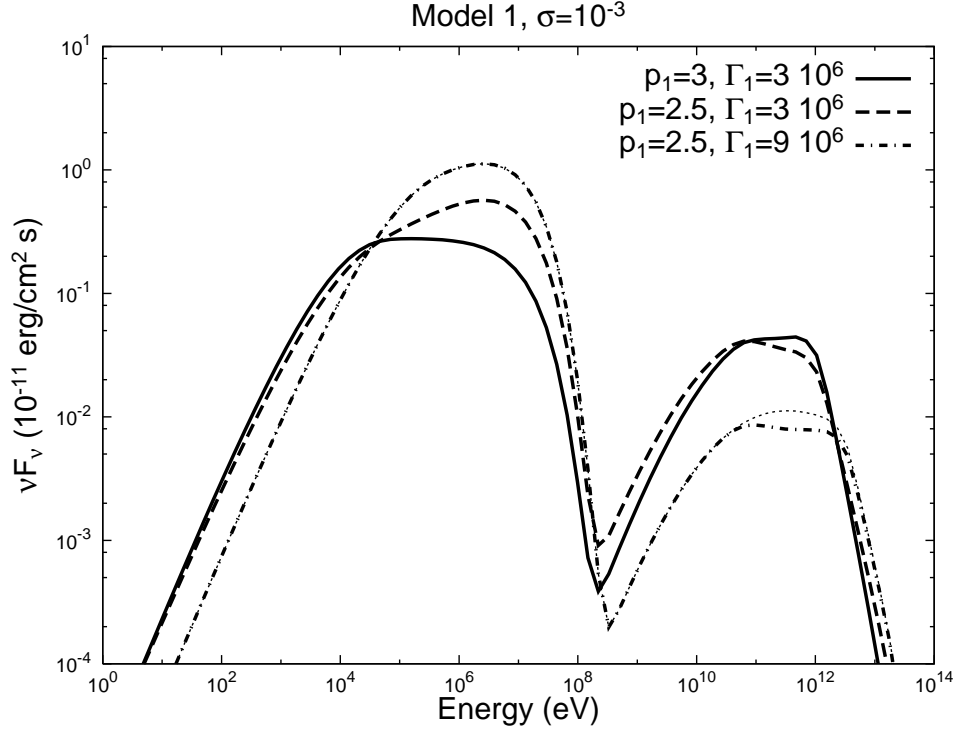


Fig. 6.— The emission spectra as a function of energy from the shocked particles at periastron. All results are for  $\sigma = 10^{-3}$  and for a shock distance calculated with Model 1. The photon index  $p_1$  and the Lorentz factor  $\Gamma_1$  are  $(p_1, \Gamma_1) = (3, 3 \times 10^6)$  for the solid line,  $(2.5, 3 \times 10^6)$  for the dashed line, and  $(2.5, 9 \times 10^6)$  for the dashed-dotted line. The thin dotted line is the result for  $(p_1, \Gamma_1) = (2.5, 9 \times 10^6)$  ignoring the effect of the pair-creation process.

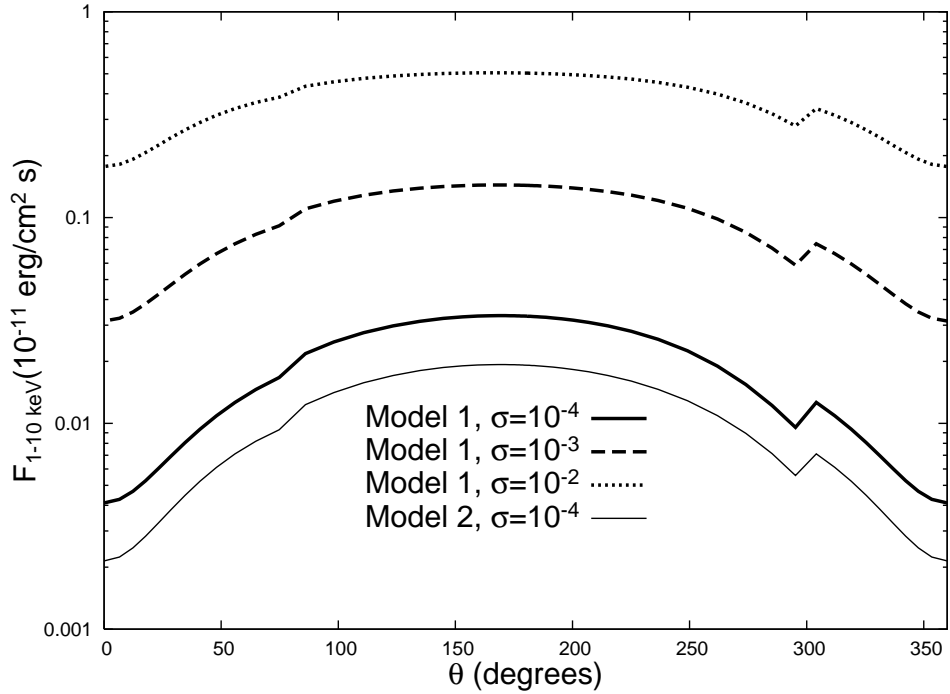


Fig. 7.— Variation of the integrated flux of the synchrotron radiation in the 1-10 keV energy band with respect to orbital phase. The thick-solid, dashed and dotted lines represents the flux for  $\sigma = 10^{-4}$ ,  $10^{-3}$  and  $10^{-2}$  with  $\dot{M}_p/f_{\Omega,p} = 10^{-8}M_{\odot} / \text{yr}$  and  $\dot{M}_e/f_{\Omega,e} = 10^{-7}M_{\odot} / \text{yr}$ . The thin-dotted line is result obtained with  $\sigma = 10^{-4}$ ,  $\dot{M}_p = 10^{-9}M_{\odot}/f_{\Omega,p} / \text{yr}$  and  $\dot{M}_e/f_{\Omega,p} = 10^{-8}M_{\odot} / \text{yr}$ . All results are for  $\Gamma_1 = 3 \times 10^6$  and  $p_1 = 2.5$ .

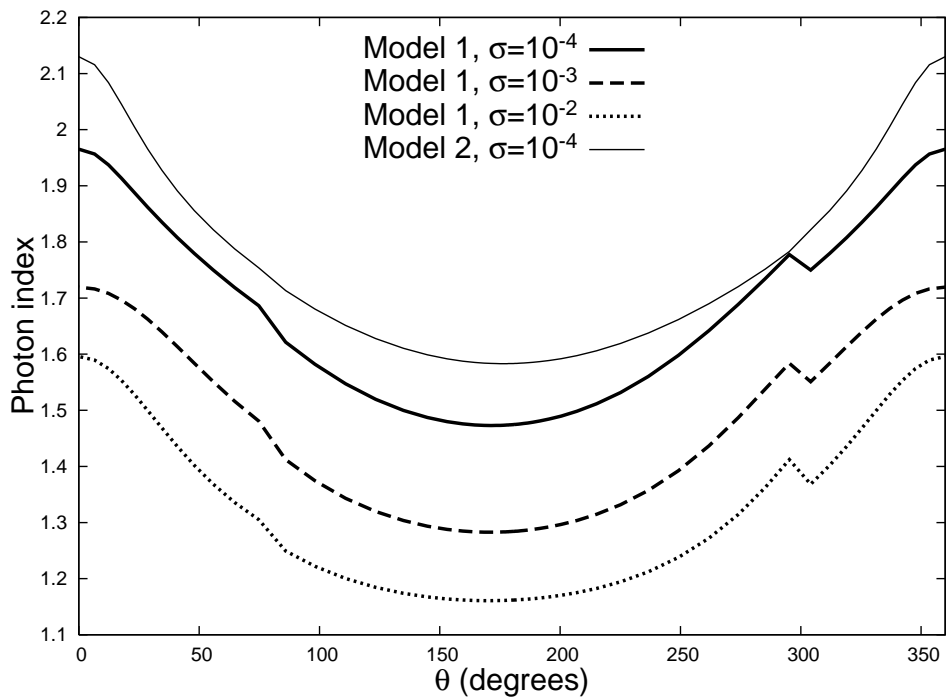


Fig. 8.— Variation of the photon index in the 1-10 keV energy band with orbital phase. The lines denote the same model parameters as in Figure 7.

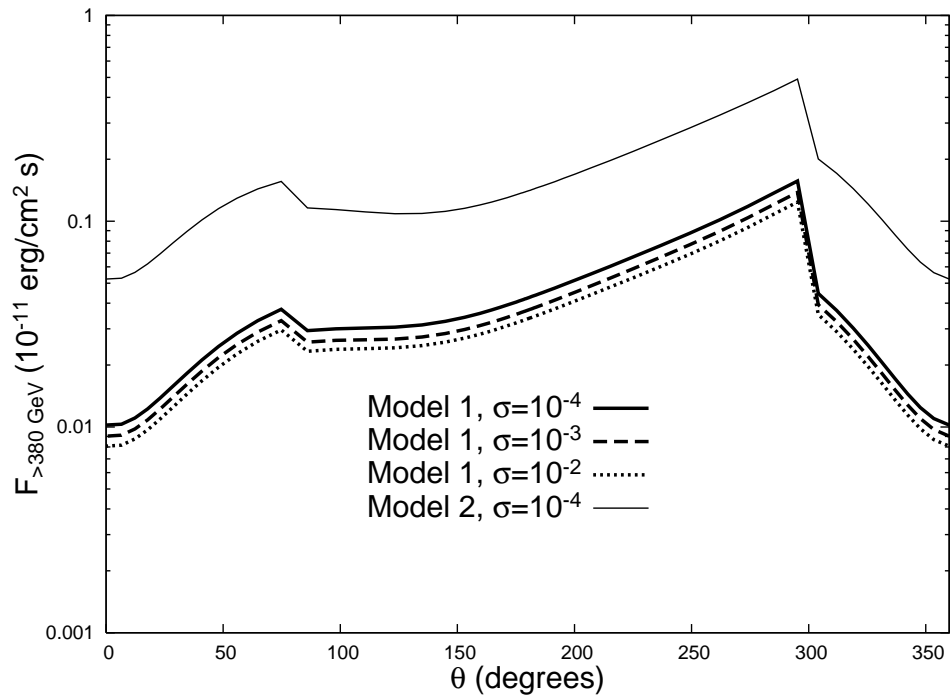


Fig. 9.— Variation of the integrated flux above 380 GeV with respect to orbital phase. The lines correspond to same case as Figure 7.

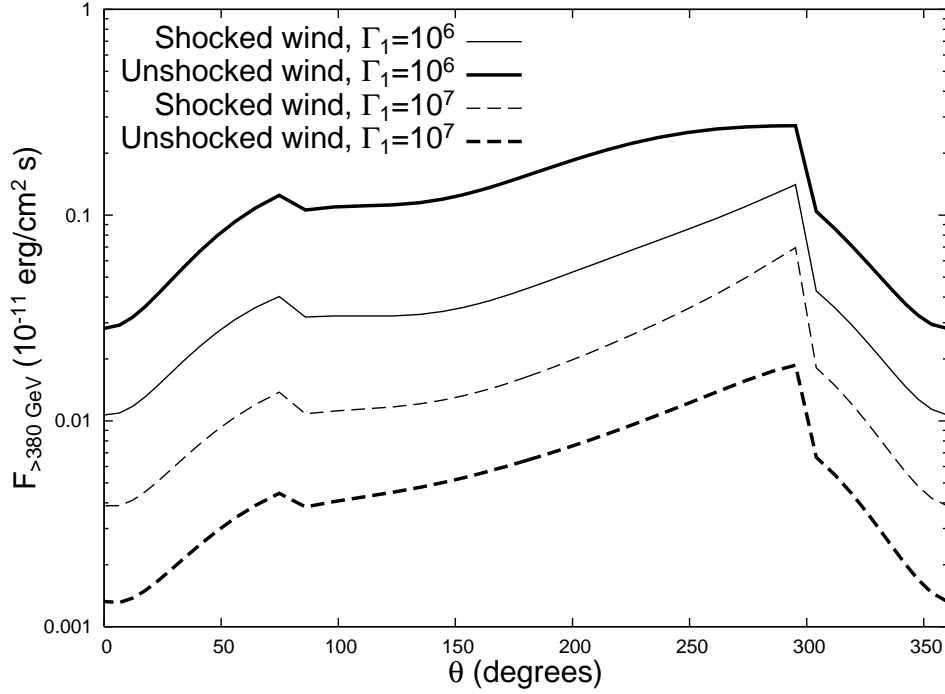


Fig. 10.— Comparison of the integrated fluxes of the very high-energy radiation from the unshocked (thick lines) and shocked (thin lines) wind as a function of the orbital phase. The solid and dashed line are the results for the mono-energetic distribution of the unshocked wind with the Lorentz factor of  $\Gamma = \Gamma_1$ . The solid and dashed lines correspond to Lorentz factors of  $\Gamma_1 = 10^6$  and  $10^7$ , respectively. All results are for  $\sigma = 10^2$ ,  $p_1 = 2.5$  for the shocked particles, and  $\dot{M}_p = 10^{-9} M_\odot / f_{\Omega,p}$  /yr and  $\dot{M}_e / f_{\Omega,p} = 10^{-8} M_\odot$  /yr.

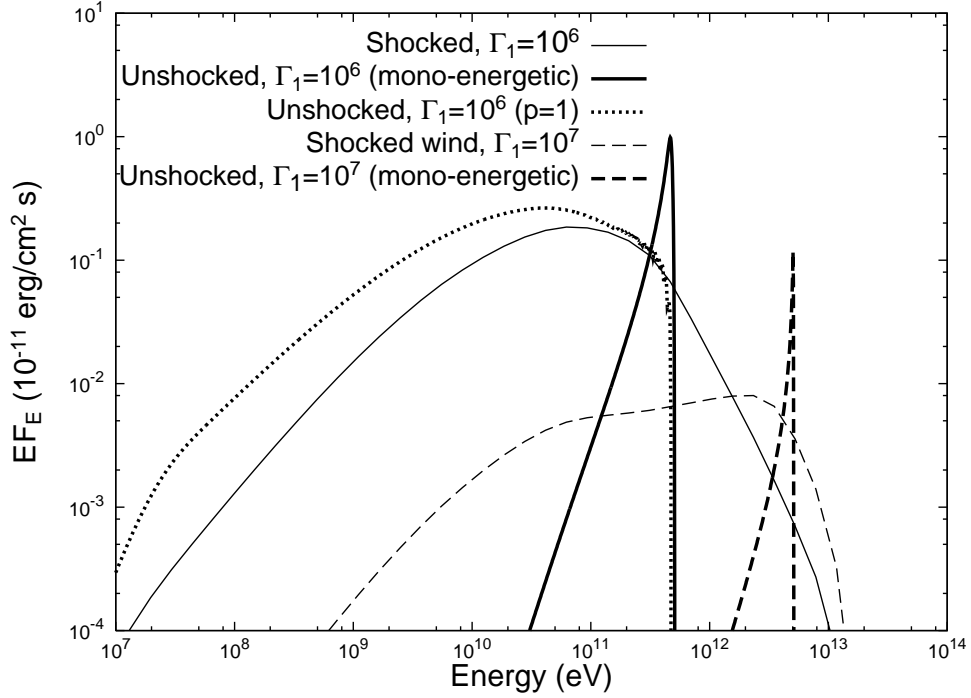


Fig. 11.— Comparison of the spectrum of the very high-energy radiation from the unshocked (thick lines) and shocked wind (thin line) at the periastron. The results are for a mono-energetic distribution of the unshocked wind with a Lorentz factor of  $\Gamma = \Gamma_1$ . The solid and dashed lines correspond to the Lorentz factor of  $\Gamma_1 = 10^6$  and  $10^7$ , respectively. The dotted line represents the spectrum of the inverse-Compton process of the unshocked particles distribution with a power law index  $p = 1$  at  $10^3 < \Gamma < 10^6$ . All results are for  $\sigma = 10^{-2}$ ,  $p_1 = 2.5$  for the shocked particles, and  $\dot{M}_p = 10^{-9} M_\odot / f_{\Omega,p} / \text{yr}$  and  $\dot{M}_e / f_{\Omega,p} = 10^{-8} M_\odot / \text{yr}$ .

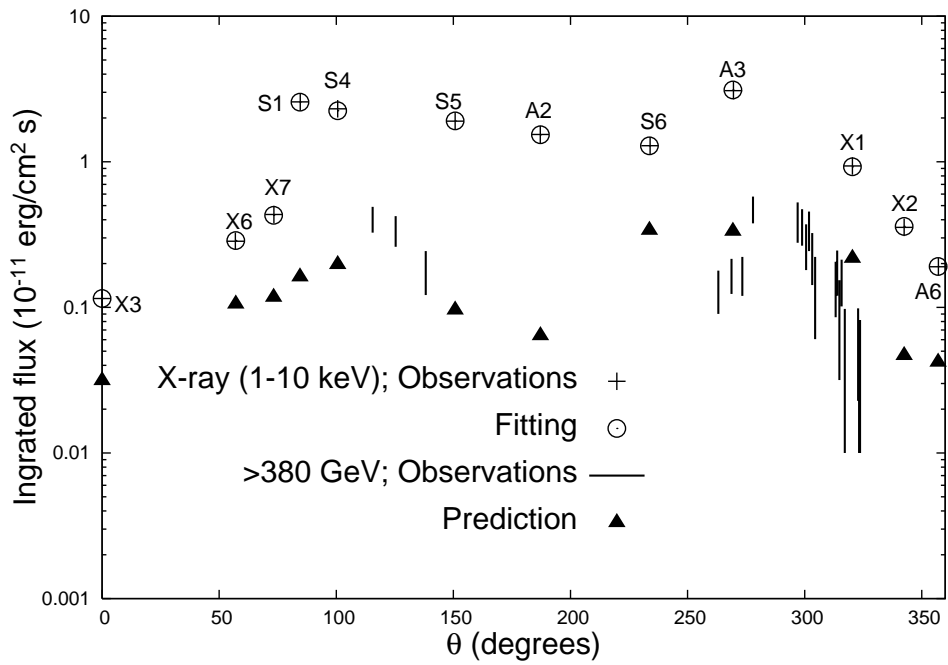


Fig. 12.— The temporal behavior of the integrated fluxes in the 1-10 keV energy band and above 380 GeV. The cross symbols are results of the fitting for the integrated flux in the 1-10 keV energy band. The filled triangles denote the predicted integrated flux above 380 GeV. The vertical lines represent the results of observations by H.E.S.S. (Aharonian et al. 2005).



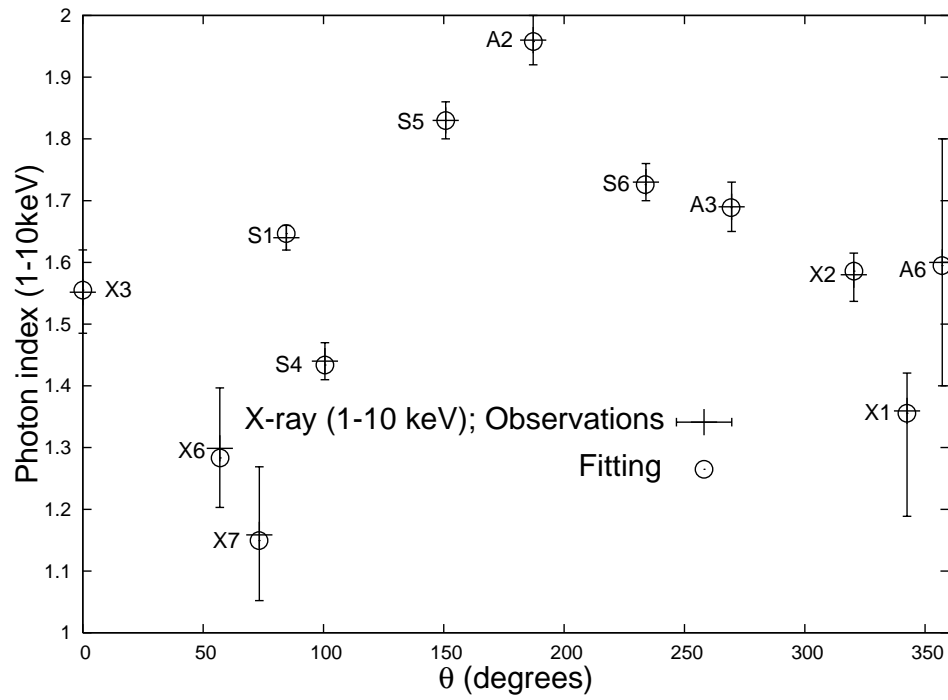


Fig. 13.— The temporal behavior of the photon index of the spectrum in the 1-10 keV energy band.

Orbital phase		X3	X6	X7	S1	S4	A5	A2	S6	A3	X1	X2	A6
Fitting parameters	$\sigma (\times 10^{-3})$	0.8	1.2	2.2	2.1	11	11	15	6.2	70	9.2	3.3	1.7
	$(p_1 = 3)$												
	$\Gamma_1 (\times 10^6)$	8.5	7.6	7.8	1.1	1.7	0.57	0.3	1	0.8	2.8	8	6.5
$F_{0.02-10^2\text{GeV}}$	$(10^{-11}\text{erg/cm}^2\text{s})$	0.017	0.1	0.19	2.3	2	5.8	12	4.3	4.8	0.46	0.028	0.028

Table 1: The fitted  $\sigma$  parameter and the Lorentz factor  $\Gamma_1$ . The results are for a power law index  $p_1 = 3$  of the electron energy distribution and for the shock distance averaged of Model 1 and Model 2 in Figure 1. The flux in the 0.02-100 GeV energy range is also listed.

Orbital phase		X3	X6	X7	S1	S4	A5	A2	S6	A3	X1	X2	A6
Fitting parameters	$\sigma$ ( $\times 10^{-3}$ )	2	5	40	40	80	9	7.5	7.9	10	25	12	5
( $\Gamma_1 = 5 \times 10^5$ )	Index $p_1$	2.1	1.62	1.45	2.35	1.99	2.8	3.2	2.57	2.55	2.2	1.72	2.2
$F_{0.02-10^2\text{GeV}}$	( $10^{-11}\text{erg/cm}^2\text{s}$ )	0.79	6.8	123	17	66	8.6	9.6	11	13	11	5.6	0.88

Table 2: The fitted  $\sigma$  parameter and the power law index  $p_1$ . The results are for a Lorentz factor  $\Gamma_1 = 5 \times 10^5$  of the electron energy distribution and for the shock distance averaged of Model 1 and Model 2 in Figure 1. The predicted flux in the 0.02-100 GeV energy range is also given.

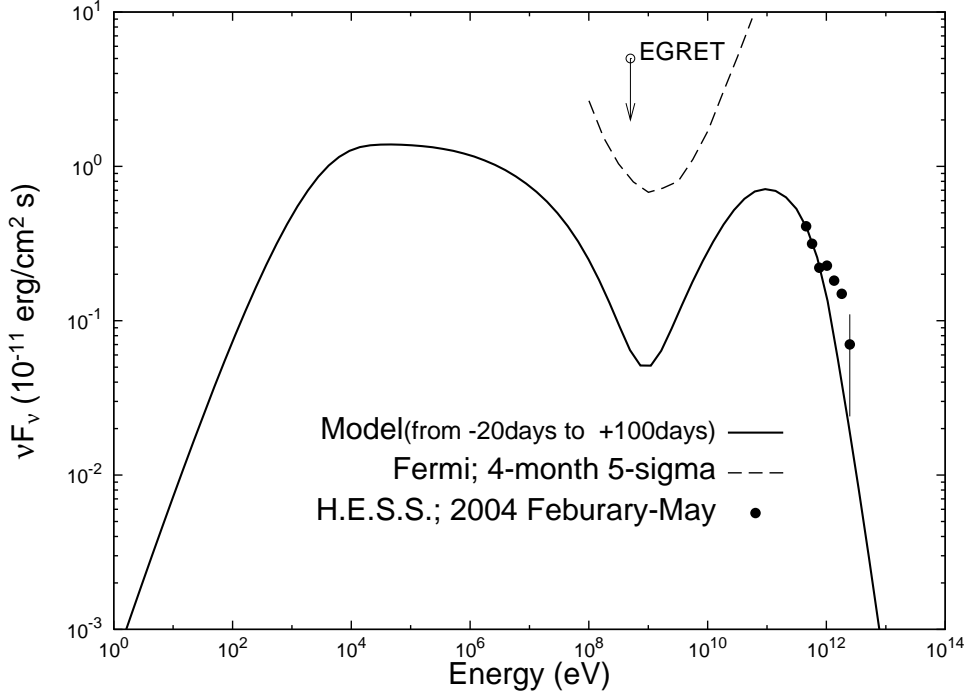


Fig. 14.— The averaged spectrum of the emission from the shocked wind during the 4 month time interval from -20 days ( $\theta \sim 83^\circ$ ) and +100 days ( $\theta \sim 324^\circ$ ). The spectrum is calculated with the model in which  $p_1 = 3$  is fixed, and  $\sigma$  and  $\Gamma_1$  vary with the orbital phase. The dashed-line represents the sensitivity for a 4-month observation using the *Fermi*, [http : //www – glast.slac.stanford.edu/software/IS/glast\\_lat\\_performance.htm](http://www-glast.slac.stanford.edu/software/IS/glast_lat_performance.htm). The filled circle is results of the observation done by H.E.S.S. during February-May, 2004 (Aharonian et al. 2005). Note that the calculated spectrum averaged during the four month time interval -60 days ( $\theta \sim 48^\circ$ ) and +60 days ( $\theta \sim 312^\circ$ ) is very similar to and can not be distinguished from the solid line. An upper limit at  $\sim 500$  MeV is obtained from EGRET observations.

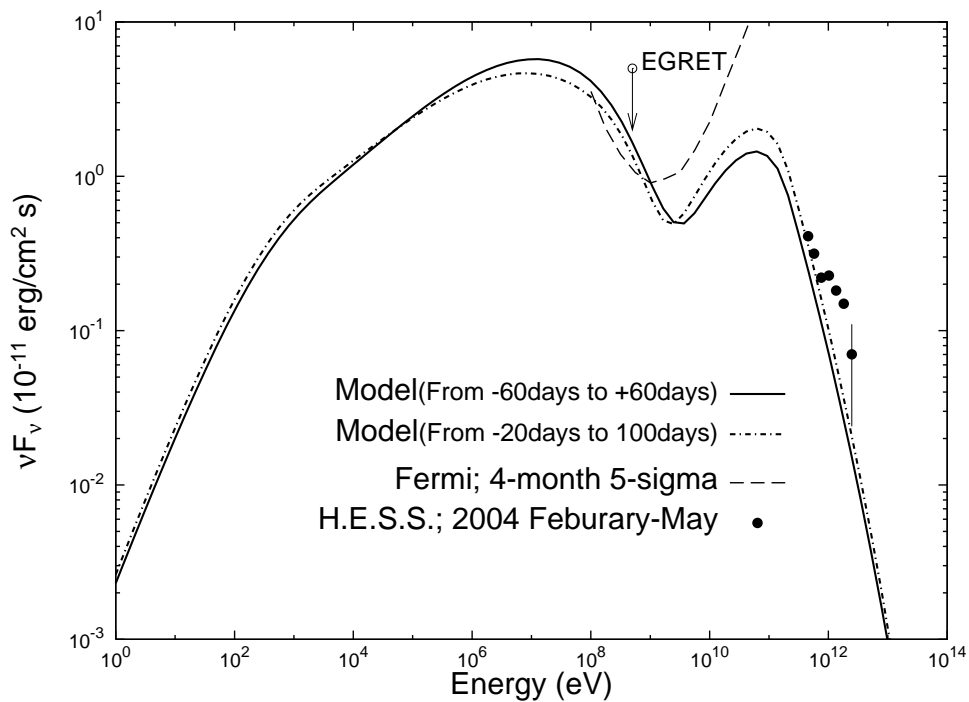


Fig. 15.— The averaged spectrum of the emission from the shocked wind during a 4 month time interval from -20 days ( $\theta \sim 83^\circ$ ) and +100 days ( $\theta \sim 324^\circ$ ) and -60 days ( $\theta \sim 48^\circ$ ) to +60 days ( $\theta \sim 312^\circ$ ). The spectrum is calculated with the model in which  $\Gamma_1 = 5 \times 10^5$  is fixed, and  $\sigma$  and  $p_1$  vary with the orbital phase. An upper limit at  $\sim 500$  MeV is obtained from EGRET observations.

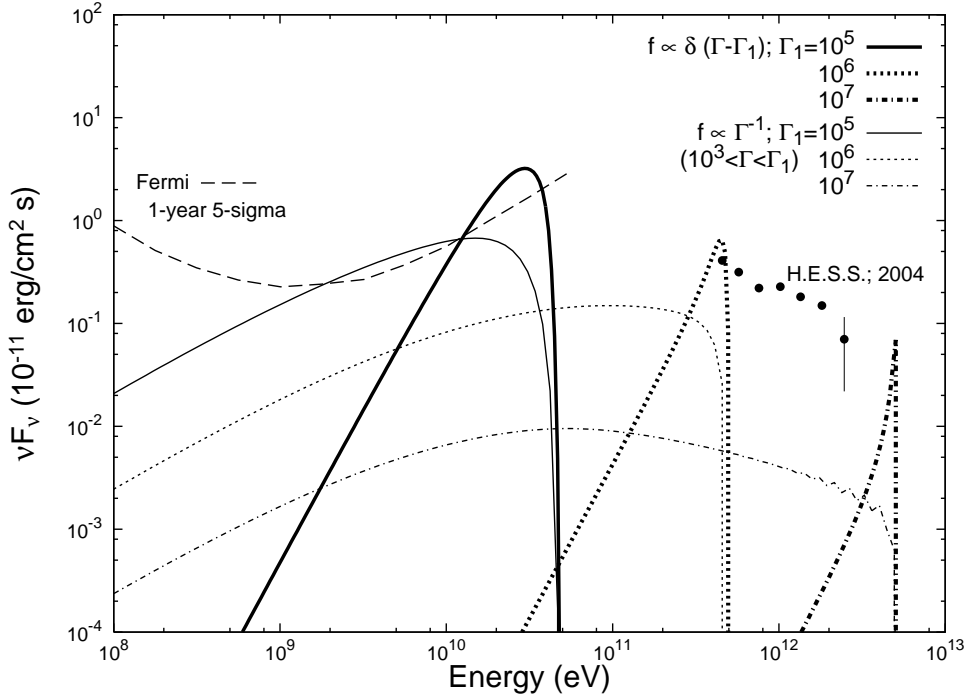


Fig. 16.— The inverse-Compton spectra from the unshocked wind. The results are for the averaged spectra during 1 year of the periastron passage. The thick and the thin lines represent the spectra from the particles with a mono-energetic distribution and a power law distribution with index  $p = 1$ , respectively. The solid, dotted and dashed-dotted lines are results for  $\Gamma_1 = 10^5$ ,  $10^6$  and  $10^7$ .